The Astrophysical Journal Supplement Series, 243:14 (24pp), 2019 July https://doi.org/10.3847/1538-4365/ab21c3

A Catalog of the Most Optically Luminous Galaxies at $z < 0.3$: Super Spirals, Super Lenticulars, Super Post-mergers, and Giant Ellipticals

Patrick M. Ogle[1], Lauranne Lanz[2], Philip N. Appleton[3], George Helou[3], and Joseph Mazzarella[3]
[1] Space Telescope Science Institute, 3700 San Martin Drive, Baltimore, MD 21218, USA; pogle@stsci.edu
[2] Dartmouth College, NH, USA
[3] IPAC, California Institute of Technology, Mail Code 220-6, Pasadena, CA 91125, USA
Received 2018 June 28; revised 2019 April 4; accepted 2019 April 8; published 2019 July 15

Abstract

We present a catalog of the 1525 most optically luminous galaxies from the Sloan Digital Sky Survey with *r*-band luminosity $L_r > 8L^*$ and redshift $z < 0.3$, including 84 super spirals, 15 super lenticulars, 14 super post-merger galaxies, and 1400 giant ellipticals. With mass in stars of $10^{11.3}$–$10^{12} M_\odot$, super spirals and lenticulars are the most massive disk galaxies currently known. The specific star formation rates of super spirals place them on or below the star-forming main sequence. They must have formed stars at a high rate throughout their history in order to grow their massive, gigantic stellar disks and maintain their blue $u - r$ integrated colors. Their disks are red on the inside and blue on the outside, consistent with inside-out growth. They tend to have small bulge-to-total (B/T) *r*-band luminosity ratios, characteristic of disk building via minor mergers and cold accretion. A large percentage of super disk galaxies (41%) have double nuclei, double disks, or other signatures of ongoing mergers. Most (72%) are found in moderate- to low-density environments, while the rest are found at the outskirts of clusters. It is likely that super spirals survive in these environments because they continue to accrete cold gas and experience only minor mergers at late times, by virtue of their enormous masses and angular momenta. We suggest that super post-mergers are the product of super spiral major mergers and may be the precursors of some giant elliptical galaxies found in low-density environments. We present two new gravitational lens candidates in an appendix.

Key words: galaxies: elliptical and lenticular, cD – galaxies: spiral

Supporting material: machine-readable tables

1. Introduction

We recently found that ∼6% of the most optically luminous galaxies at redshift $z < 0.3$ are giant, high-surface-brightness spiral galaxies, with masses of 10^{11}–$10^{12} M_\odot$ and isophotal diameters of 55–140 kpc (Ogle et al. 2016). These super spiral galaxies are actively forming stars and appear to be vastly scaled-up versions of normal spiral galaxies. The extreme sizes, masses, and luminosities of super spirals extend the parameter space over which galaxy scaling laws may be studied, providing a new arena to test theories of massive galaxy formation and evolution.

In addition to giving new insights into galaxy formation and growth, super spirals can help discriminate among proposed mechanisms for quenching star formation in massive galaxies. The red optical colors of massive spiral galaxies may indicate that they are starved of gas and dying (Bamford et al. 2009; Masters et al. 2010; Schawinski et al. 2014). However, it is important to determine for any individual galaxy whether its red colors indicate low specific star formation rate (SSFR) or dust extinction via mid-infrared (MIR) photometry (Fraser-McKelvie et al. 2016). Star formation is thought to be quenched in most galaxies above a mass in stars of $\sim 10^{11} M_\odot$, by collisions, active galactic nucleus (AGN) activity, accretion shocks, or ram pressure stripping, which turn them into red and dead elliptical or lenticular galaxies (Dekel & Birnboim 2006; Hopkins et al. 2006; Elbaz et al. 2007; Martig et al. 2009; Schawinski et al. 2014; Chang et al. 2015). Though they are rare, the existence of super spirals demonstrates that the limit to spiral galaxy size and mass is much higher than previously thought, and that high mass in stars cannot be the primary cause of star formation quenching. In fact, spiral galaxies with mass in stars $\sim 10^{11} M_\odot$ may be the most efficient at converting gas into stars, with mass fractions in stars approaching the cosmological baryon fraction (Posti et al. 2019). Super spirals and giant ellipticals may represent distinct evolutionary pathways for the most massive galaxies, depending on dark halo mass and angular momentum. Super spirals may remain unquenched because they reside in less massive dark halos than giant ellipticals of similar mass in stars.

Hydrodynamical simulations that include increasingly realistic star formation and AGN feedback prescriptions (Springel & Hernquist 2005; Governato et al. 2007; Hopkins et al. 2009) show that galaxy mergers play a key role in determining the configuration, dynamics, star formation histories, and ultimate fates of galaxies. Simulations also reveal that typically half of the mass in stars is acquired via mergers, while the rest is formed in situ (Rodriguez-Gomez et al. 2016). A relatively large fraction of super spirals have two bulges surrounded by a common spiral disk or tidal features (Ogle et al. 2016), demonstrating the importance of mergers for these most massive disk galaxies. However, super spirals may survive most mergers because of their extremely large masses and sizes. That is, for a super spiral, even a merger with a typical L^* galaxy is a high-mass-ratio, minor merger that will not destroy its massive disk.

This work extends the search for the most massive, optically luminous galaxies, relaxing the restriction that they be detected in the near-ultraviolet (NUV) band by the *Galaxy Evolution Explorer (GALEX)*, with the goal of understanding how super spirals relate to other types of massive galaxies. We present a new class of super lenticular galaxies that may be quenched super spirals and a new class of super post-merger galaxies that may be the product of super spiral major mergers.

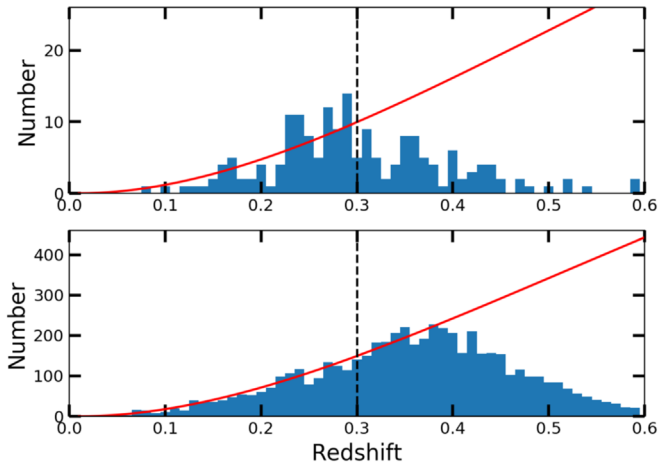

Figure 1. Redshift distributions for galaxies with $L_r > 8L^*$. Top: super disk (spiral and lenticular) redshift histogram compared to a constant comoving density curve. Bottom: giant elliptical redshift histogram. The Ogle et al. Galaxy Catalog is limited to $z < 0.3$ (dashed line). The distribution for ellipticals extends to higher redshift because they are augmented by the SDSS luminous red galaxy sample.

2. Sample and Photometry

2.1. Sample Selection

Our galaxy sample is primarily selected for high Sloan Digital Sky Survey (SDSS) r-band luminosity ($L_r > 8L^*$), which is an excellent tracer of mass in stars for unobscured galaxies. Unlike Ogle et al. (2016), here we do not impose requirements of *GALEX* NUV-band detection or spiral morphology, resulting in a sample that also includes lenticular, elliptical, and peculiar galaxies, and which is less biased toward high SFRs. We selected all galaxies from the NASA/IPAC Extragalactic Database (NED) with an existing spectroscopic redshift $z < 0.3$ and r-band photometry from SDSS I or II (York et al. 2000; Strauss et al. 2002). These galaxies were then ranked by their r-band monochromatic luminosities (L_r), after correcting for Galactic extinction and applying a K-correction. We report L_r relative to the characteristic luminosity at the knee of the galaxy luminosity function of $L^* = 5.41 \times 10^{43}$ erg s^{-1} at 6200 Å (Blanton et al. 2003).

The redshift distribution for spiral galaxies with $L_r > 8L^*$ cuts off at $z = 0.30 \pm 0.02$ (Figure 1), corresponding to the SDSS I/II spectroscopic selection limit of $r = 17.77$ (Strauss et al. 2002). The distribution of elliptical galaxies cuts off at a higher redshift of $z = 0.38 \pm 0.01$, corresponding to the effective redshift cutoff of the SDSS luminous red galaxy (LRG) sample (Eisenstein et al. 2001). Therefore, to mitigate against incompleteness and selection effects at greater redshifts, we restrict the present study to SDSS galaxies with $L_r > 8L^*$ at $z < 0.3$.

We found 1616 candidate galaxies at $z < 0.3$ with $L_r > 8L^*$, presented as the Ogle et al. Galaxy Catalog (OGC: Tables 2–5). We visually inspected the SDSS three-color images to determine their morphologies and checked their redshifts against their SDSS spectra. Galaxies were classified as spiral, lenticular, elliptical, or peculiar, based on visual appearance. In particular, relative prominence of bulge and disk components and presence of spiral arms were the key discriminants. We give a breakdown of OGC galaxy types in Table 1. A total of 1525 galaxies are legitimate high-luminosity galaxies. The remaining 91 galaxies that have inaccurate photometry (51 in Table 3), or incorrect redshifts (24 in Table 4), or that overlap with foreground objects (16 in Table 5) are excluded from further analysis.

Table 1
OGC Galaxy Type Percentages

Type	Subtype	Number	Percentage
Super disk		99	6.5
	Spiral	84	5.5
	Lenticular (S0/Sa)	15	1.0
Giant elliptical		1400	91.8
Post-merger		14	0.9
Bright AGN		12	0.8
Luminous galaxies		1525	100.0
Rejects		91	
All		1616	

Apart from constructing a manageable sample of the most optically luminous galaxies, there is no particular physical significance to our $8L^*$ cutoff. As we shall demonstrate, super spirals are dramatically scaled-up versions of much more abundant L^* spirals, albeit with some significant structural, photometric, and other differences. Since our $8L^*$ limit is somewhat arbitrary, the search for superluminous, giant spiral galaxies could be extended down to lower luminosities. For example, there are 16,301 SDSS galaxies with $L_r > 5L^*$ at $z < 0.25$. Using this $5L^*$ cutoff would yield galaxies in the top 2% of the r-band luminosity distribution, compared to the top 0.2% for our adopted $8L^*$ cutoff.

2.2. Super Spirals

We find 84 super spiral galaxies with $L_r > 8L^*$ at $z < 0.3$ (Table 6; Figures 11 and 12). This includes 32 new super spirals, augmenting our original sample of 53 (Ogle et al. 2016). Inspection of an archival *Hubble Space Telescope* (*HST*) image (see Appendix A.1) led us to remove OGC 0302, reducing the sample size from 85 to 84.

In order to compare morphologies (Figure 2), we cross-matched the OGC with the Galaxy Zoo DR1 catalog (Lintott et al. 2011). We find that only 22/84 super spirals (26%) are classified as spirals with $P_{\rm spiral} > 0.8$ by Galaxy Zoo, 10 are classified as ellipticals (12%), 50 are classified as uncertain (60%), and two (OGC 0574 and 586) are not classified (2%). Super spirals with uncertain Galaxy Zoo classification include galaxies that appear to have normal spiral morphologies, such as OGC 0065 and 0713 ($P_{\rm spiral} = 0.57$ and 0.60), and spirals that are disturbed by mergers, such as OGC 0789 and 1304 ($P_{\rm spiral} = 0.61$ and 0.29). It appears that the Galaxy Zoo classifications of many super spirals are rendered uncertain by their relatively high redshifts (Bamford et al. 2009) and high merger fraction.

The mean number density of super spirals in our sample is 58 Gpc^{-3} within a comoving volume of 7.14 Gpc^3, corrected for the 20.3% sky coverage of SDSS II. This is 5.5% of the total number density of high-luminosity galaxies in our sample (1050 Gpc^{-3}). Correcting for an inclination incompleteness of 40% (Section 5), the number density of super spirals increases to 97 Gpc^{-3}, 9.2% of the population of galaxies with $L_r > 8L^*$.

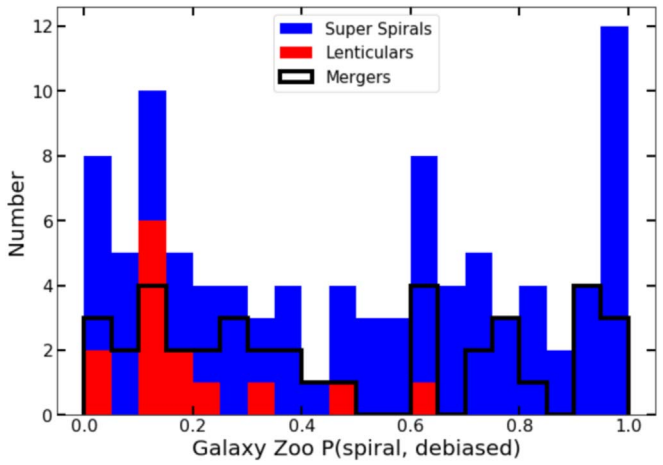

Figure 2. Galaxy Zoo 1 debiased spiral probability (Bamford et al. 2009), corrected for redshift bias. Because the redshift bias corrections are large for galaxies at $z > 0.08$, and spiral galaxies at these redshifts may be misclassified as early type, Galaxy Zoo morphologies should be interpreted with caution. Total bar height indicates total spirals and lenticulars, while color represents the fraction of each type. The black histogram shows the number of mergers, regardless of morphological type.

We emphasize that super spiral galaxies are one of the rarest galaxy populations in the universe. Their comoving number density is a factor of 10^3–10^4 lower than samples of massive galaxies constructed from smaller surveys at higher redshift (e.g., Davari et al. 2017; Faisst et al. 2017). Existing deep surveys are not large enough to yield significant numbers of super spirals. Deeper large surveys by *Euclid*, the *Wide Field Infrared Survey Telescope*, and the Large Synoptic Survey Telesope will be necessary to discover and characterize super spiral progenitors at $z > 1$.

Extending our search for high-luminosity SDSS galaxies to $0.3 < z < 0.6$ yields 83 additional super spirals (included in Figure 1 but not tabulated). The redshift distribution of super spirals falls off at $z > 0.3$, corresponding to the SDSS I/II magnitude limit for spectroscopy and our $L_r > 8L^*$ luminosity lower limit.

2.3. Super Lenticulars and Giant Ellipticals

Ogle et al. (2016) predicted a new class of super lenticular galaxies, but for the most part they were excluded from their sample due to an NUV-band selection criterion. Here we identify 15 super lenticular (S0/Sa) galaxies with $L_r > 8L^*$ at $z < 0.3$ (Table 6; Figures 11 and 12). It is easiest to identify lenticulars at intermediate inclination (Section 5), where they are less likely to be confused with ellipticals or edge-on spirals. Based on the small number in our sample, the space density of super lenticulars is >10 Gpc^{-3}. It is likely that we are missing $>60\%$ of super lenticulars, at both low and high inclination, based on the distribution of observed inclinations (Section 5).

There are 1400 giant elliptical galaxies in the OGC, which constitute 91.8% of the sample. Their mean comoving number density is 970 Gpc^{-3}, corrected for SDSS II sky coverage. The most optically luminous giant elliptical galaxy is OGC 0021 (2MASX J12220526+4518109), with $L_r = 19.8L^*$. It resides at the center of a rich galaxy cluster, which is frequently (but not always) the case for the giant ellipticals in our sample.

2.4. Super Post-mergers and Luminous AGN Hosts

There are 14 peculiar galaxies (0.9% of the sample) that have disturbed morphologies, indicative of recent mergers (Table 6 and Figure 13). We highlight one additional peculiar starburst galaxy (OGC 1662, $L_r = 7.9L^*$) which does not quite make our $8L^*$ cutoff but has a very peculiar morphology and multi-hued appearance. We include all of these galaxies in our photometric analysis, but differentiate them from galaxies with more regular morphologies.

We exclude 12 non-spiral galaxies (0.8% of the sample) that are quasar hosts, blazar hosts, or contain bright stars seen in projection from further analysis because an AGN or foreground star is likely to contribute a significant fraction of the luminosity at wavelengths of interest (Table 7 and Figure 13).

2.5. Photometry

We use CModel catalog photometry from SDSS DR6 (York et al. 2000) and aperture photometry from the Two Micron All Sky Survey (2MASS; Skrutskie et al. 2006) and the *Wide-field Infrared Survey Explorer* (*WISE*; Wright et al. 2010) to estimate the total optical luminosities, mass in stars, and SFRs. The smallest 2MASS and *WISE* apertures that encompass the D_{25} isophotal diameter at $r = 25$ mag were selected. The SDSS CModel magnitudes are effectively aperture-matched and are therefore appropriate for measuring integrated galaxy color. All galaxies are detected in the SDSS u, g, r, i, z bands. A total of 90 super disk galaxies are detected in the 2MASS K_s band and 86 in the $W3$ band. Of the 1400 giant ellipticals, 127 are undetected in the K_s band, and 128 are undetected in $W3$.

We correct SDSS and 2MASS photometry for Galactic extinction using the NED extinction calculator, based on the Galactic extinction maps of Schlafly & Finkbeiner (2011). We K-correct SDSS and 2MASS magnitudes to rest-frame values with a simple, custom procedure that performs log-linear interpolation of the observed spectral energy distribution (SED). We K-correct *WISE* magnitudes using two representative model SEDs, one for star-forming galaxies with $W2 - W3 > 2$, and a second for quiescent galaxies with $W2 - W3 \leqslant 2$, yielding K-corrections of $K(W3) < 0.33$ mag and $K(W2 - W3) < 0.21$ over the redshift range of our sample.

3. Mass in Stars and SFR

The SEDs of nearly all galaxies in our sample are dominated by stellar populations at NUV to NIR wavelengths, and warm dust emission at MIR wavelengths. Galaxies with SEDs dominated by AGNs (0.8% of the sample) are excluded from this analysis. We estimate mass in stars (Figure 3) from K-corrected 2MASS K_s magnitude and K-corrected SDSS $u - r$ color, using the prescription of Bell et al. (2003), with a small correction (+0.004 dex) to convert to a Chabrier (2003) initial stellar mass function. The mass estimates are relatively insensitive to both dust extinction and variations in mass-to-light ratio M/L with mean stellar population age.

The super spiral masses are on average four times larger than those given by Ogle et al. (2016), primarily because of a systematic error they made converting from K_s-band monochromatic luminosity to solar luminosity units. The K_s monochromatic luminosity was incorrectly divided by the solar bolometric luminosity, rather than the solar K_s-band monochromatic luminosity, which is a factor of 5.5 smaller. This is partially offset by the new K-corrections to the K_s band magnitudes,

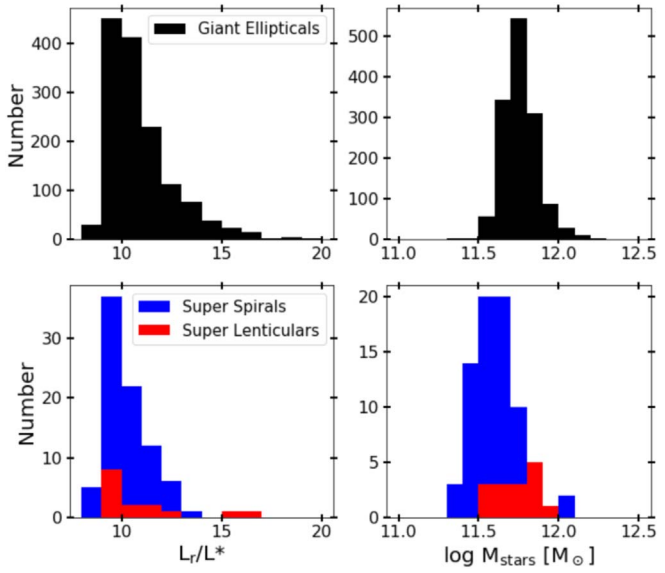

Figure 3. Luminosity and mass of giant ellipticals compared to super disks. Left: *r*-band luminosity distributions. Right: distributions of mass in stars.

which also act to reduce the scatter in the distribution of masses in stars. These new, more accurate estimates lead to a better understanding of how truly massive super spirals are. They in turn affect the SSFRs and location of super spirals relative to the star-forming main sequence (SFMS; Figure 4), shifting them to the right by 0.6 dex and placing most of them on or below this relation.

We compare the masses in stars of super disk galaxies and giant ellipticals in Figure 3. The narrow range of high *r*-band luminosities in the OGC effectively selects for the most massive galaxies, with masses in stars of $10^{11.3}$–$10^{12.3}$ $M_\odot$. The mean mass in stars is a factor of 1.4 (0.14 dex) smaller for super spirals than for super lenticulars and giant elliptical galaxies, because of their systematically lower stellar M/Ls. A major merger between a super spiral and another massive galaxy could potentially create super lenticular and giant elliptical galaxies of greater mass. Super spiral major mergers may provide a channel to create giant elliptical galaxies outside of galaxy clusters, like the most massive isolated elliptical OGC 0078 (2MASX J02295551 +0104361), with $\log M_{\rm stars} = 11.9$. However, the dark halo masses of isolated giant ellipticals like this one are likely to be considerably smaller than the dark halo masses of giant ellipticals in clusters, even though they have comparable masses in stars. The very different evolutionary histories of ellipticals in the most massive halos versus those that form from super spiral mergers may potentially result in different fractional mass in stars, gas content, kinematics, and morphology.

We estimate SFRs from *K*-corrected *WISE* *W*3-band (12 μm) fluxes, which trace warm dust heated by UV photons in star-forming galaxies (Chang et al. 2015).[4] We plot SFR against mass in stars for OGC galaxies in Figure 4. This method gives consistent SFR values for star-forming galaxies compared to full-SED fitting with MAGPHYS (da Cunha et al. 2008; Ogle et al. 2016) and is relatively insensitive to dust extinction, compared to SFRs estimated from UV or Hα emission. On the other hand, old stellar populations contribute most of the *W*3-band luminosity for quiescent elliptical galaxies with the lowest SSFRs (Bressan et al. 2006; Chang et al. 2015), so their SFRs should be considered to be upper limits. Between these two extremes, both old and young stellar populations will contribute to the *W*3 luminosity. Assuming a baseline *WISE* color of $W2 - W3 = 0.32$ for quiescent ellipticals, the break-even point (equal *W*3 luminosity from star formation and old stars) occurs at $W2 - W3 \simeq 0.32 + 2.5 \log 2 = 1.07$ (Figure 5). Only seven super spirals, three super lenticulars, and one super post-merger have $W3 - W2$ colors bluer than this, such that their *W*3 luminosity is dominated by old stellar populations. Dust heated by A-type stars in recently quenched galaxies may also lead to an overestimate of the SFR (Alatalo et al. 2014, 2017). This is not the case for most super disk galaxies in our sample, though it may be a concern for the peculiar, post-merger galaxies, depending on the fractions of UV photons from A stars and star-forming regions.

The super spirals and super lenticulars have SFRs ranging from 1 to 30 $M_\odot$ yr^{-1} (Figure 4). Their SSFRs span a broad range from (0.02–1.5) $\times$ 10^{-10} yr^{-1} (1/SSFR = 6–500 Gyr), with most falling on or below the SFMS, extrapolated from less-luminous SDSS spiral galaxies. There appears to be a continuum of massive, super disk galaxies, from active star-forming super spirals to quiescent super lenticulars, similar to the well-established sequence for L^* galaxies. There is no sharp dividing line between super spirals and super lenticulars in the $M_{\rm stars}$–SFR plane. Because super spirals are so massive, not even those with the highest SFRs and IR luminosities are global starbursts. Based on SDSS spectra, we do find strong *nuclear* starbursts in five super spirals (OGC 0217, 0454, 1457, 1464, and 1520) and relatively strong Hα from nuclear star formation in two (OGC 1312, and 1512).

The giant ellipticals are for the most part quiescent, with SSFR $< 1.5 \times 10^{-11}$ yr^{-1}. While a small number (14) have greater SSFRs than this, they are not starbursts. Six of these (OGC 0034, 0087, 0123, 0792, 1412, and 1581) have high Balmer line equivalent widths and significant populations of young, blue stars in their SDSS spectra. The dust and UV emission from the vast majority of more quiescent giant ellipticals may indicate a low level of ongoing star formation accompanied by young stellar populations.

Most of the super post-mergers (11/14) have SSFRs that formally put them on the SFMS. However, they have SDSS spectra with high Hδ equivalent widths characteristic of dominant A-star populations in post-starburst galaxies. The *W*3-band fluxes may therefore have a significant contribution from warm dust heated by UV emission from post-starburst stellar populations (Melnick & De Propris 2013; Alatalo et al. 2017). NUV emission from A–F-type stars can linger for 1–3 Gyr following starburst activity, leading to significant MIR emission. The post-mergers display a range of Hα equivalent widths from star formation and AGN activity, indicating that they are still forming stars and feeding their black holes. Only one (OGC 0792) has an SDSS spectrum that indicates an ongoing burst of nuclear star formation. Five have clear AGN signatures in their SDSS spectra, including two (OGC 0247 and 1413) with high-luminosity AGNs that contribute significantly to their *W*3-band luminosity and red $W1 - W3$ colors. We may be viewing most of these peculiar galaxies during quenching episodes immediately following gas-rich

[4] Note that there is a known offset of −0.22 dex (Chang et al. 2015) between SFRs derived from *WISE* measurements compared to those derived from Hα fluxes (Brinchmann et al. 2004; Elbaz et al. 2007). We adopt the SFMS of Elbaz et al. (2007), shifted downward by −0.22 dex to match *WISE*-estimated SFRs.

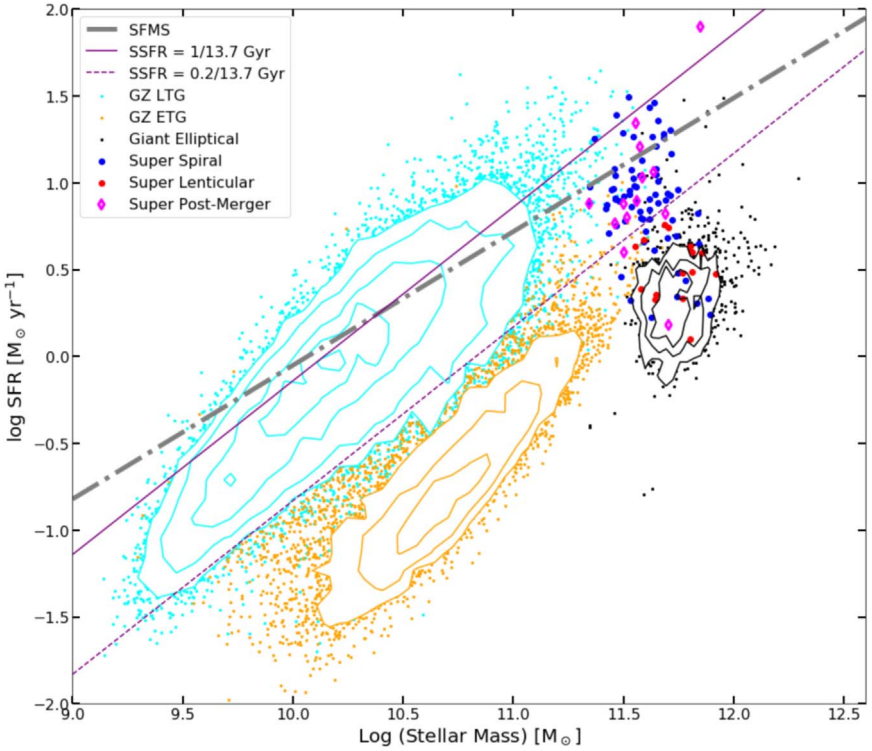

Figure 4. Star formation rates (SFRs) and masses in stars of super disks, post-mergers, and giant ellipticals compared to Galaxy Zoo late-type and early-type galaxies (GZ LTGs and ETGs: Alatalo et al. 2014; Schawinski et al. 2014; see the legend). The thick dotted–dashed line indicates the star-forming main sequence at $z \sim 0$ (Elbaz et al. 2007), which has been shifted downward by 0.22 dex to match the *WISE*-based SFR estimates of Chang et al. (2015). The dashed and solid purple lines indicate specific SFRs of (0.2–1)/(13.7 Gyr), a range where active star-forming galaxies would double their masses in stars in one to five times the current age of the universe.

mergers, where the observed AGN activity may eventually clear out much of the remaining gas. If all of the star-forming super post-mergers in our sample are the result of super spiral major mergers, we estimate a per-galaxy super spiral destruction rate of $0.16\,\mathrm{Gyr}^{-1}$, assuming a post-merger settling timescale of 1.0 Gyr (Lotz et al. 2008). The two super post-mergers (OGC 0743 and 1141) with SDSS spectra and SEDs characteristic of predominantly old stellar populations may be the product of dry mergers.

4. Colors

4.1. Total System Colors

For lower-mass galaxies with $M_{\rm stars} = 10^9$–$10^{11} M_\odot$, there is a well-established bimodal distribution in color between blue, star-forming spiral galaxies and red elliptical galaxies with low SFR (Schawinski et al. 2014). Galaxies that fall in the so-called green valley that separates the two populations are primarily disk galaxies (spirals and lenticulars) with relatively low specific SFRs, plus a small contingent of elliptical galaxies with modest SFRs (Figure 5). The origin of the bimodal color distribution has been attributed to various star formation quenching mechanisms, including galaxy mergers and quasar activity.

Most super spirals are blue, with rest frame $u - r < 2.2$ mag, similar to less-massive Galaxy Zoo late-type galaxies (Lintott et al. 2008). The *WISE* $W2 - W3$ color tracks SSFR, to the extent that it correlates with $K_s - W3$, the basis of our SFR versus mass plot (Figure 4). Super spirals with red $W2 - W3$ color have high SSFR, while lenticulars have relatively low SSFR and bluer $W2 - W3$ color. We find a linear anti-correlation between $W2 - W3$ and $u - r$ for our sample of massive galaxies (Figure 5(a)), reflecting an anti-correlation between SSFR and luminosity-weighted mean stellar population age. Galaxies with the highest SSFR have blue $u - r$ and red $W2 - W3$, characteristic of luminous, young stellar populations, while galaxies with lower SSFR have redder $u - r$ and bluer $W2 - W3$ color, from a mix of young and old stellar populations. This stands in contrast to lower-mass disk galaxies along the blue sequence, which follow a dog-leg trajectory in color space (Figure 5(a)). The $W2 - W3$ color for these galaxies remains red even after they have quenched and moved into the green valley, perhaps because of dust heated by a post-starburst population of A stars (Alatalo et al. 2014, 2017). Super spirals do not appear to follow this trajectory in color space, indicating a different evolutionary history that is consistent with ongoing star formation and a mixture of old and young stellar populations. We can reproduce the observed range of SDSS and *WISE* colors by a linear mix of a young, star-forming stellar population ($u - r = 1.4$, $W2 - W3 = 3.8$) with an old, quiescent stellar population ($u - r = 2.65$, $W2 - W3 = 0.32$), where we vary the star-forming mass fraction $f_{\rm sf}$ (Figure 5(a)). This allows us to estimate the star-forming mass fraction for any given galaxy, and the fraction of light in each band that comes from the two stellar populations. This model does not apply to quenching galaxies, such as lower-mass lenticulars, which follow a different trajectory in this color space.

While super spirals have similar colors to less massive spirals, they stand dramatically apart in the color–mass plane (Figure 5(b)). Most super spirals have blue $u - r$ colors corresponding to high SSFRs, in spite of their enormous mass in stars. In order to better understand the stellar populations of

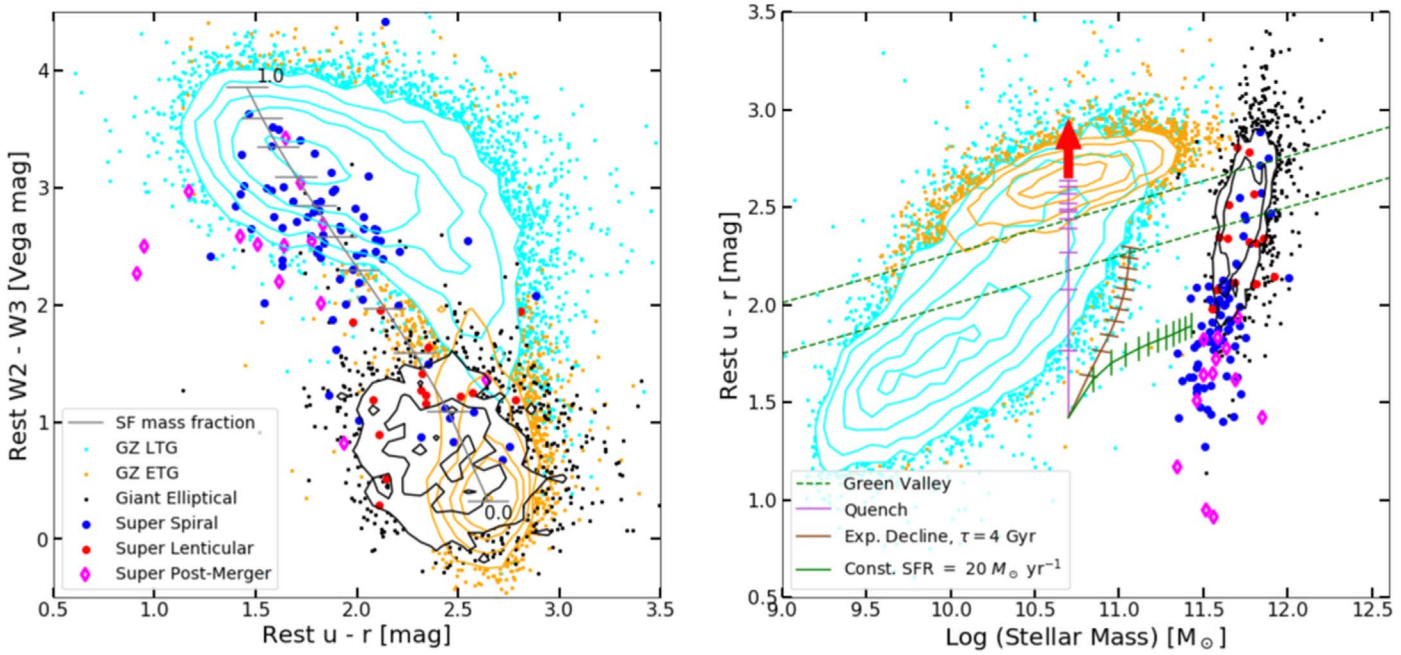

Figure 5. (a) SDSS and *WISE* colors of super spirals (dark blue), super lenticulars (red), super post-mergers (magenta diamonds), and giant ellipticals (black) compared to Galaxy Zoo (GZ) classified SDSS galaxies at $z = 0.02$–0.05 (Lintott et al. 2008; Alatalo et al. 2014; Schawinski et al. 2014). Reddening by Galactic-type dust would increase $u - r$, with no effect on the *WISE* color. The gray track follows the linear mixing of a young, star-forming stellar population ($u - r = 1.4$, $W2 - W3 = 3.8$) with an old, quiescent stellar population ($u - r = 2.65$, $W2 - W3 = 0.32$). The star-forming fraction f_{sf} by $W2$ luminosity, which follows mass in stars, is indicated by the tick marks separated by 0.1. The mix with $f_{sf} = 0.1$ has $W2 - W3 = 1.09$ and equal contributions to $W3$ luminosity from quiescent and star-forming populations. (b) SDSS color–mass diagram, without any correction for internal extinction. The location of the green valley (green dashed lines), as determined for less massive galaxies by Schawinski et al. (2014), is shown for comparison. We over-plot evolutionary tracks based on Bruzual & Charlot (2003) stellar population synthesis models, with a starting age of 0.5 Gyr and markers spaced 1 Gyr apart (tick marks at color ages of 1.5, 2.5, …11.5 Gyr). All three galaxies start at $z = 6$ with $\log M_{stars} = 10.7$, solar metallicity $Z = Z_{\odot}$, and a stellar population age of 0.5 Gyr, which represents the newly formed bulge. In the quench model (lavender track), the galaxy quenches immediately. For the other two models, a disk subsequently forms with either constant SFR (green track) or exponentially declining SFR (brown track) with e-folding timescale of $\tau = 4$ Gyr. Galaxy $u - r$ color gets redder with time even for the constant SFR model as old stellar populations accumulate. The endpoint mass, color, and bulge/disk mass ratio of the constant SFR model is similar to super spirals in our sample. The red arrow indicates the effect on $u - r$ of increasing the end-point metallicity by 0.2 dex to $1.6Z_{\odot}$.

super spirals and lenticulars, we created synthetic galaxy colors by summing the stellar population synthesis (SPS) spectral models of Bruzual & Charlot (2003). We assume solar metallicity ($Z = Z_{\odot}$) for the massive galaxies in our sample. The influence of the mass–metallicity relation in star-forming galaxies (e.g., Tremonti et al. 2004) on $u - r$ is also examined by increasing the end-point metallicity by 0.2 dex to $1.6Z_{\odot}$, the maximum value supported by the SPS models. For a constant or declining SFR, the $u - r$ color reddens monotonically with time, yielding a range of color that matches super spirals (Figure 5(b)). In particular, galaxies that form stars at a constant rate become steadily redder with time as old stars accumulate within their disks, reaching $u - r = 1.8$ mag after 12 Gyr. Galaxies that are redder than this must have declining SFRs. Increasing the metallicity by 0.2 dex to $Z = 1.6Z_{\odot}$ reddens $u - r$ by 0.25 mag in our SPS models.

Both super lenticulars and massive ellipticals are on average redder than super spirals, consistent with older stellar population ages. For a single stellar population created in a δ-function burst, the $u - r$ color increases from $u - r = 1.4$ mag at $t = 0.5$ Gyr to $u - r = 2.7$ mag at $t = 11.5$ Gyr in our SPS quench model (Figure 5(b)). This type of evolution describes passive galaxies on the red sequence that formed and quenched not long after the big bang. We introduce the color age t_{color}, appropriate to such a single burst stellar population, in order to characterize the average-luminosity-weighted stellar population ages of galaxies. The giant ellipticals have a median $u - r$ color of 2.5 mag, indicating $t_{color} \sim 5.5$ Gyr, compared to less-massive Galaxy Zoo early-type galaxies that have a median $u - r$ color of 2.7 mag and $t_{color} \sim 11.5$ Gyr. The bluer colors and younger color ages of the massive ellipticals in our sample may indicate that they are more susceptible to bouts of renewed star formation, perhaps as a result of more frequent mergers or cooling flows in dense environments (Egami et al. 2006; Burns et al. 2008).

4.2. Color Gradient

The disks of spiral galaxies typically display a negative color gradient, with bluer colors at larger radii, attributed to a combination of decreasing stellar population age and decreasing metallicity with radius (de Jong 1996; Bell & de Jong 2000). While a gradient in dust extinction can also in principle cause a color gradient, this would require an unrealistically large optical depth and dust scale height (de Jong 1996).

We performed elliptical aperture photometry on the SDSS images of one of the brightest, nearby super spirals (OGC 0543) to characterize its radial color profile (Figure 6). The integrated, K-corrected color over the full galaxy is $u - r = 2.03$ mag, typical for the massive star-forming galaxies in our sample. The r- and i-band radial light profiles, which track mass in stars, are smoother and drop more quickly than the u-band profile, which tracks star formation. Oscillations in the g-band surface brightness correspond to spiral arms in the stellar disk. The $u - r$ color is bluer in the nucleus than in the

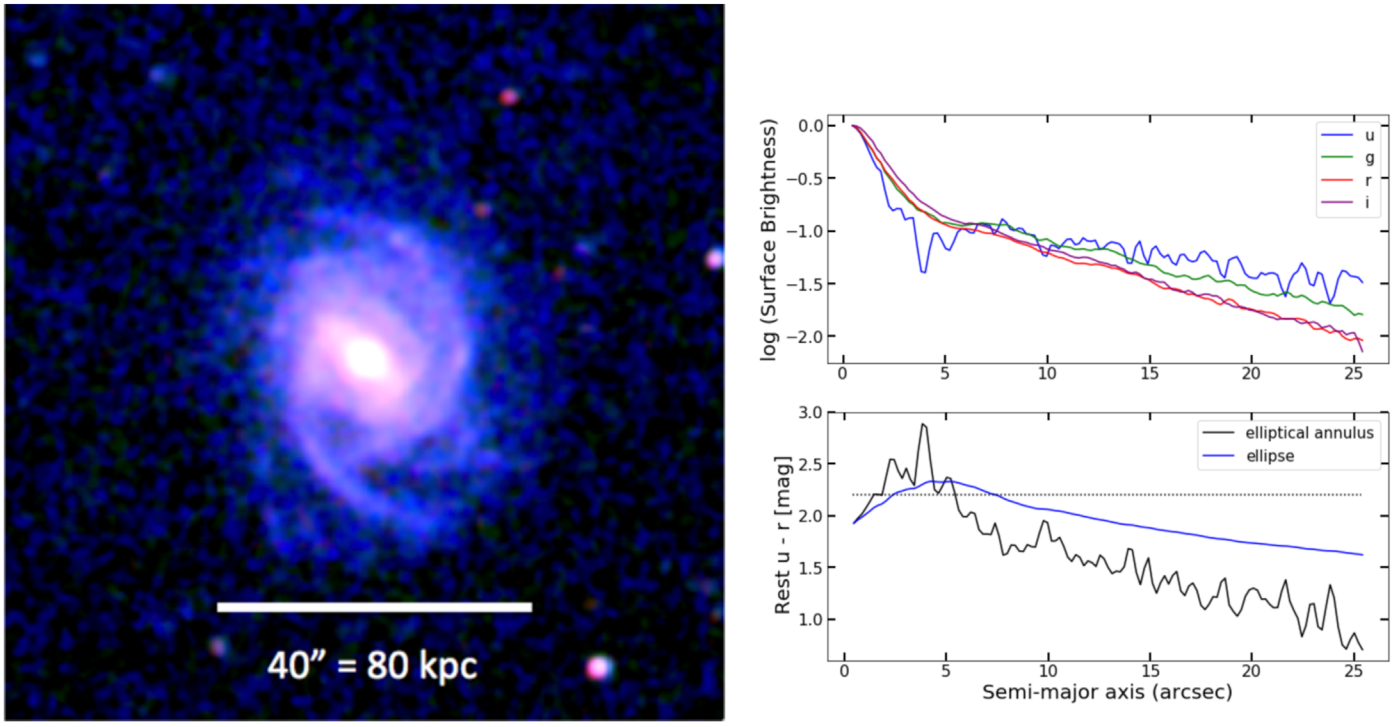

Figure 6. Image: super spiral OGC 0543 SDSS *gri* 3-color image. Top plot: surface brightness profile in SDSS bands, within elliptical annuli, normalized to unity at $r = 0''$. Bottom plot: K-corrected $u - r$ color (solid black line) decreases with radius in the disk, indicating increasing specific SFR and decreasing color age or decreasing metallicity. The integrated $u - r$ color within an elliptical aperture (solid blue line) also becomes bluer as the aperture size is increased. The optical color separator for the massive blue- and red-sequence galaxies in our sample ($u - r = 2.2$ mag) is indicated by the dotted line.

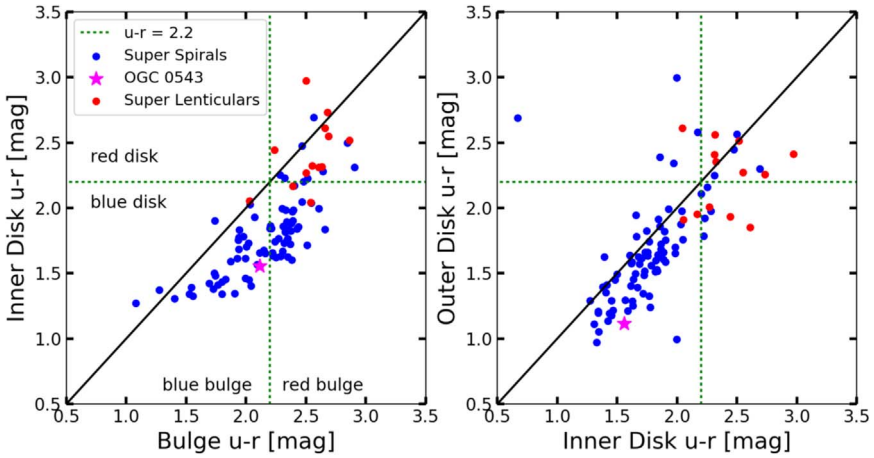

Figure 7. Radial $u - r$ color gradients for super spirals (blue points) and super lenticulars (red points). Left: the inner disks (middle one-third elliptical annulus) of super spirals and super lenticulars are systematically bluer than their bulges (inner one-third ellipse). Right: the outer disks (outer one-third annulus) of super spirals are systematically bluer than their inner disks (middle one-third elliptical annulus), indicating younger stellar populations. The diagonal (black line) delineates equal $u - r$ color. The horizontal and vertical dotted lines at $u - r = 2.2$ mag separate red and blue stellar populations. The data point for our super spiral case study subject, OGC 0543 (Figure 6) is plotted as the star symbol.

inner disk because of AGN activity (OGC 0543 has a Seyfert 1 nucleus). Outside of the nucleus, the $u - r$ color gets progressively bluer with increasing radius in the disk, indicating increasing SSFR and decreasing color age with radius. The large range in $u - r$ color seen in the disk of OGC 0543 spans the full range of integrated $u - r$ color for spiral galaxies (Figure 5(b)). The u-band surface brightness profile indicates a current SFR that declines gradually (by only 0.5 dex) from $6''$ to $25''$ (12–60 kpc). The exponential r-band radial profile over the same interval indicates that a larger surface density of old stars has accumulated in the inner disk over cosmic time, relative to the outer disk. This is consistent with inside-out growth via gas accretion (possibly accompanied by some inward migration of old stars).

We measured the surface brightness and color profiles in elliptical annuli at fixed PA for all super spirals and super lenticulars in our sample, to see if they show similar color gradients to OGC 0543. We summarize our results by comparing the integrated $u - r$ color inside three annuli, with outer semimajor axes of 0.33, 0.66, and 1.0 times the isophotal radius at $r = 25$ mag, R_{25} (Figure 7). We label these three regions bulge, inner disk, and outer disk, though it should be

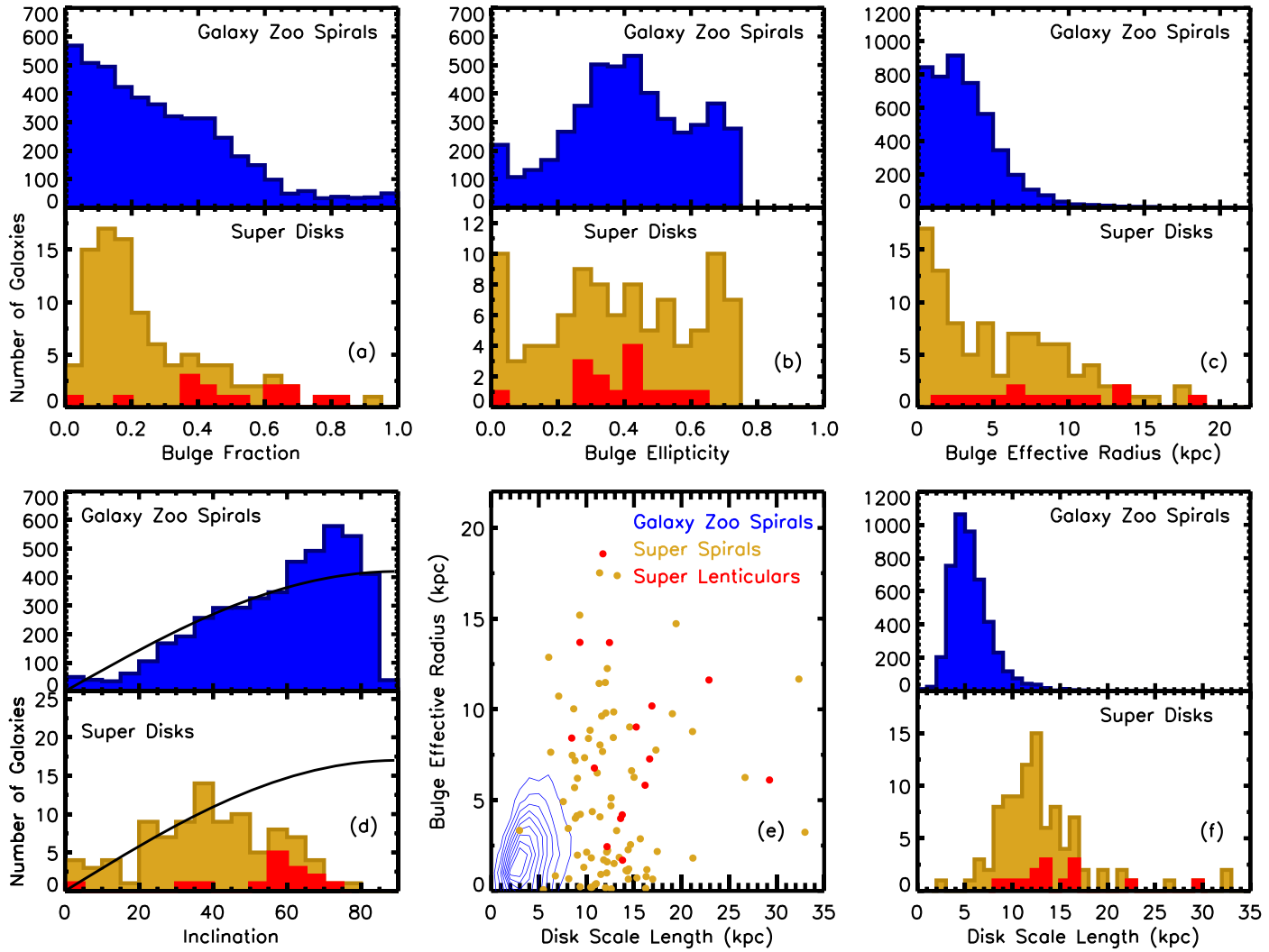

Figure 8. Distributions of super spiral (gold histograms) and super lenticular (red histograms) bulge-plus-disk decomposition parameters, as measured by Simard et al. (2011), compared to Galaxy Zoo spirals (blue histograms): (a) bulge to total (B/T) r-band luminosity fraction, (b) bulge ellipticity e, (c) bulge effective radius R_e, (d) disk inclination distribution compared to the sin(i) expectation for randomly oriented disks (black curve), (e) bulge effective radius vs. disk scale length, and (f) disk exponential scale length.

kept in mind that all three regions may contain flux contributions from the bulge, pseudo-disk, disk, or stellar bar.

As expected, the inner disks of super spirals are bluer than their bulges (Figure 7(left)). Super lenticulars have systematically redder bulges and disks than super spirals, consistent with older stellar populations and lower SSFR. We can divide super disk galaxies (spirals and lenticulars) into three categories, based on the $u - r$ colors of their inner disks and bulges, which can be tied to a range of different star formation histories. Forty-five percent have blue disks and blue bulges, 42% percent have blue disks and red bulges, and 13% percent have red disks and red bulges. The first category corresponds to galaxies with star-forming disks and bulges, the second to star-forming disks and quiescent bulges, and the third to quiescent disks and bulges. The very bluest bulges (possibly pseudo-bulges) with $u - r < 1.7$ mag have color ages of $<$1.5 Gyr, indicating recent star formation. Red disks with $u - r > 2.2$ mag and color ages $>$3.5 Gyr have quenched star formation, including both lenticulars and red spirals like those found in Galaxy Zoo (Bamford et al. 2009).

The outer disks of super spirals are on average 0.2 mag bluer in $u - r$ compared to their inner disks (Figure 7(right)). This is consistent with the color gradient found for OGC 0543 above, confirming a tendency for a younger stellar population age (or lower metallicity) in the outer disks of super spirals. Although still quite red, the inner disks of super lenticulars are systematically bluer than their bulges, consistent with younger color ages and later quenching times. Their outer disks show no systematic difference in $u - r$ color with respect to their inner disks.

5. Bulge–Disk Decomposition

We use GIM2D bulge–disk decompositions from Simard et al. (2011) to compare the quantitative morphologies and sizes of super spirals and super lenticulars to Galaxy Zoo spirals (Figure 8). In these decompositions, the bulge is fit by an $n = 4$ Sérsic profile with ellipticity e and effective radius R_e, while the disk is fit by an exponential profile with scale length R_d and inclination i. We confirm the results of Ogle et al. (2016) with our larger sample.

The mean bulge-to-total r-band luminosity ratio (B/T) is smaller for super spirals than for Galaxy Zoo spirals (Figure 8(a)). The super spiral B/T distribution peaks at $B/T = 0.1$–0.2, while there is no clear peak in the B/T distribution for Galaxy Zoo spirals. The B/T distribution of Galaxy Zoo spirals has a tail with $B/T > 0.7$, where the disk contributes a minor fraction of the r-band flux. Only one super spiral (OGC 1514) falls in this part of the distribution. Otherwise, our visual morphological identification of super spirals is consistent with B/T values indicating a large disk component. All but two super lenticulars (OGC 0044 and 1386) have $B/T > 0.35$, consistent with a major merger origin.

The distribution of bulge ellipticity (Figure 8(b)) is similar for super spirals and Galaxy Zoo spirals. Many super spirals ($20 \pm 5\%$) appear to have bars (Table 6). While the bar fraction is low compared to the total bar fraction of 65% for L^* spiral galaxies at $z = 0.14$–0.47 measured with the *HST* (Sheth et al. 2008), it is consistent with the strong bar fraction of 27% for the same set of galaxies (dropping to 20% for spirals with the smallest B/T). The lower spatial resolution of SDSS compared to *HST* may cause us to miss the weak bars in our sample. Higher spatial resolution imaging is needed to improve on our measurement of the bar fraction in super spirals. The mean bulge ellipticity for barred super spirals is $\langle e \rangle = 0.50 \pm 0.08$, compared to $\langle e \rangle = 0.38 \pm 0.02$, for non-barred super spirals. It is likely that the presence of a bar increases the fit bulge ellipticity in some cases.

Both bulges and disks are on average larger in super spirals and super lenticulars than in Galaxy Zoo spirals (Figures 8(c), (e), (f)). The disk scale lengths of super spirals extend to much larger values than those of Galaxy Zoo spirals. The distributions peak at $R_d = 12.5$ kpc and $R_d = 4.5$ kpc, respectively. The distribution of bulge effective radius also extends to much larger values for super disks than for Galaxy Zoo spirals. However, a significant fraction of super spirals (36/99) have small, unresolved bulges with $R_e < 2$ kpc in spite of their large disk scale lengths (>5 kpc). Both super spirals and super lenticulars cover a large range in R_e/R_d, perhaps reflecting a range in merger histories and merger mass ratios.

Even though we dropped the NUV-band selection criterion of Ogle et al. (2016), we still find a large deficit of super spirals at inclinations $i > 50°$, compared to both Galaxy Zoo spirals and the expected distribution for randomly oriented disks (Figure 8(d)). Roughly 40% of super spirals must have dropped out of the parent sample because dust extinction in their highly inclined disks caused their r-band luminosities to fall below our selection threshold of $L_r > 8L^*$. An additional extinction of $\Delta r = 0.6$ mag would suffice to move the brightest face-on super spiral (OGC 0065) below our luminosity selection threshold. The most luminous edge-on spiral galaxy in SDSS I/II at $z < 0.3$ is 2MFGC 12344 ($z = 0.1407$), with inclination $i = 81°$. Its dust lane crosses just above its nucleus, consistent with its high inclination (Figure 9). Its apparent luminosity ($L_r = 7.9$) is just below our sample selection threshold, and its r-band isophotal diameter (120 kpc) rivals the largest super spiral in our sample (OGC 0139: $D = 134$ kpc, $L_r = 13.4$). Selection by NIR luminosity may help to recover many more of these edge-on, dust-obscured super spirals. Super lenticulars are preferentially selected at intermediate inclinations of 50°–75°, because face-on lenticulars are difficult to distinguish from ellipticals, and because edge-on lenticulars may be misclassified as spirals. We attribute the similar excess of Galaxy Zoo spirals at inclinations of 60°–80° to a population of lenticulars.

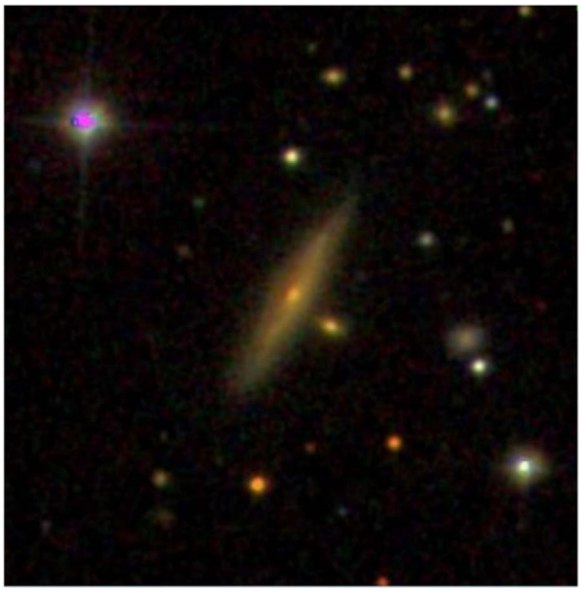

Figure 9. SDSS image of 2MFGC 12344, the most luminous nearly edge-on spiral galaxy in SDSS I/II. The field of view is 250 kpc on a side.

6. Environment

Most super spirals and super lenticulars are found in moderately dense environments (Figures 14 and 15), with an average of 7.8 ± 0.3 SDSS galaxies within a projected radius of 150 kpc. In comparison, OGC giant ellipticals have on average roughly twice as many galaxies within the same radius (14.5 ± 0.1). We find only eight super spirals in dense environments with 14 or more apparent companions within a projected radius of 150 kpc: OGC 0299, 0586, 0799, 1023, 1304, 1329, 1457, and 1559. While most companions are more than 1 magnitude fainter than the super spiral, some are potentially massive enough to result in a major, disruptive merger (e.g., companions to OGC 0299, 0799, 1304, and 1457).

We searched for known galaxy clusters and groups within 2′ of each super spiral, using NED (Table 8). We find that 28% of super spirals and super lenticulars appear to be associated with clusters or groups of galaxies (Table 8). For these, we used the NED Environment Search tool to count the number of galaxies with separations and redshifts that put them within 1 Mpc and 500 km s^{-1} (N1) or within 10 Mpc and 5000 km s^{-1} (N10). While these numbers give a rough sense of cluster richness, they must be quite incomplete for galaxies at the highest redshifts. Most cluster or group members would not be luminous enough to make it into the SDSS spectroscopic sample. Indeed, it is seen that clusters associated with the lowest redshift super spirals have the most SDSS redshifts (e.g., 310 for OGC 1559 at $z = 0.186$), while candidate clusters associated with super spirals at the highest redshifts have fewer SDSS redshifts (e.g., 23 for OGC 044 at $z = 0.293$). Deeper redshift surveys are necessary to measure the richness and velocity dispersions of the highest-redshift candidate clusters.

For four super spirals in the richest clusters (OGC 0345, 0516, 1268, and 1304), we generated velocity plots with NED Environment Search (e.g., Figure 10). The locations of the super spirals within the velocity distributions confirm that they

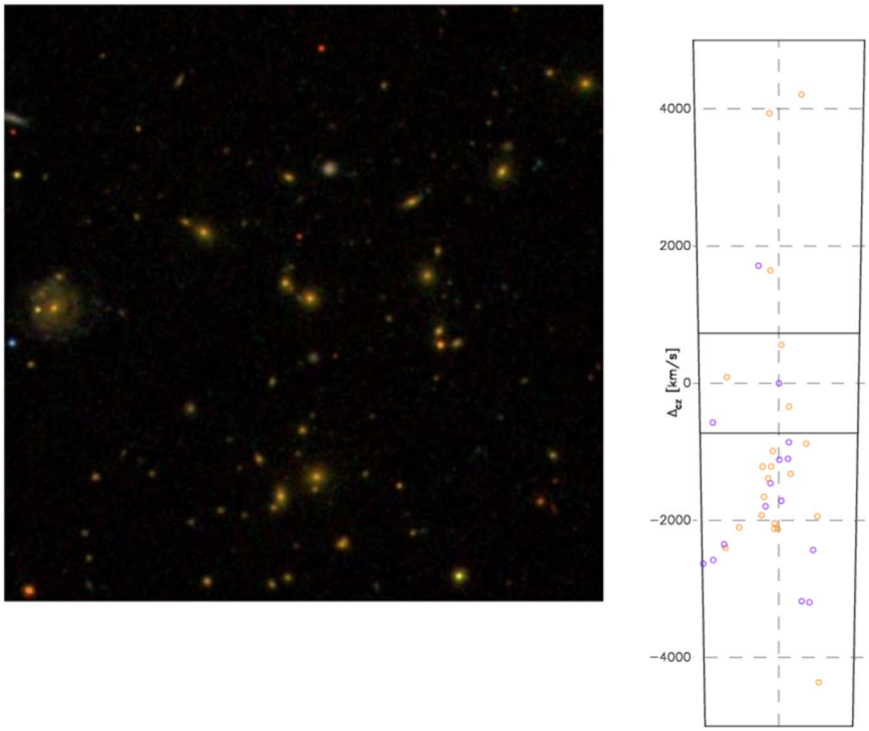

Figure 10. Left: super spiral OGC 0345 (at left edge) in galaxy cluster WHL J092608.1+240524. The SDSS image is 200″ = 716 kpc on a side. Right: position–velocity diagram from NED Environment Search, 10 Mpc wide and centered on OGC 0345. Orange and purple correspond to galaxies above and below the plane of OGC 0345, respectively.

are either cluster or supercluster members. The large velocity dispersions of these clusters (full range of ±3000 km s^{-1}) indicate that they are very massive. However, no super spirals reside at cluster centers, and their velocities relative to the mean cluster redshift are large (∼2000 km s^{-1}). This indicates that these super spirals did not form at the cluster center of mass, but rather in the outskirts. This is confirmed for four super spiral bright cluster galaxies (BCGs; OGC 0170, 0345, 1268, and 1304) recently observed with *XMM-Newton* by Bogdan et al. (2018), which turn out to be located at large distances (150–1100 kpc) from the X-ray centroids of their host clusters. However, one super lenticular that they observed (OGC 0073) does turn out to be located at the center of a low-mass ($M_{500} = 10^{14} M_{\odot}$) galaxy cluster.

The presence of some super spirals in clusters is consistent with their high mass in stars and likely high halo mass. Super spirals may form preferentially in regions of the universe with relatively high overdensities, where a lot of gas is available to accrete onto their dark matter halos. On the other hand, a location at the periphery rather than the center of clusters is consistent with the morphology–density relation. We would not expect super spiral galaxies to survive as long as they have if they were at the centers of massive clusters, where they would be subject to frequent harassment by cluster galaxies.

7. Galaxy Mergers

Many super spirals and super lenticulars (41%) appear to be involved in mergers (Table 9). There are 14 candidate interacting pairs or triples with projected separations of 28–131 kpc and 27 advanced mergers with either double nuclei or overlapping disks with projected separations between 4 and 32 kpc. Only three of these pairs are spectroscopically confirmed (OGC 0044, 0299, and 0984). The remaining double nuclei, double disks, and interacting companions need to be verified spectroscopically to rule out chance alignments, but their appearance is quite suggestive of dynamical interactions. Many of them are highly distorted or have tidal tails or debris that confirm their merger status. We find seven candidate collisional ring galaxies (Table 9) and two galaxies with asymmetric, ν-shaped arms (OGC 0290 and 1423). We find four additional galaxies with three or more arms that we do not classify as mergers (OGC 0256, 0926, 1046, and 1323), which may also have suffered a recent dynamical disturbance.

A high merger percentage is expected for galaxies as massive as super spirals and super lenticulars. Hopkins et al. (2010) estimate that galaxies with $M_{\rm stars} = 10^{12} M_{\odot}$ experienced on average 1.5 major mergers with mass ratio $\mu > 0.3$ and 5.5 minor mergers with $0.1 < \mu < 0.3$ since $z = 2$, based on halo occupation statistics. Most mergers experienced at late times by such massive galaxies are minor mergers because equally massive companions are quite rare. The fraction of massive galaxies with currently visible ongoing mergers can be estimated from the merger rates predicted by their model, multiplied by the merger visibility timescale. They predict a $\mu > 0.1$ merger rate of 0.2 Gyr^{-1} at $M_{\rm stars} = 10^{11} M_{\odot}$, increasing to 2 Gyr^{-1} for $10^{12} M_{\odot}$ galaxies at $z = 0.3$. For a merger visibility timescale of 1.0 Gyr, the corresponding merger fraction ranges from 0.2 to 1.0. This is roughly consistent with the observed super spiral merger fraction of 0.41 and merger rate of 0.4 Gyr^{-1}, for a median galaxy mass of $10^{11.6}\ M_{\odot}$. If the 11/14 star-forming super post-mergers in our sample are also the product of super spiral major mergers, this gives a destructive major-merger fraction of 0.12 and rate of 0.12 Gyr^{-1}, assuming a post-merger settling timescale of 1.0 Gyr (Lotz et al. 2008). During this settling time, obvious tidal signatures of the merger will disappear, and the $u - r$ color of the

post-merger $u - r$ color will redden by 0.35 mag to $u - r = 1.75$ mag (Figure 5), at which point it will be difficult to distinguish from other quenched giant ellipticals in our sample. Including 38 ongoing super spiral mergers and 11 star-forming super post-mergers, and excluding super lenticular mergers, yields an overall star-forming merger fraction of 0.52 and merger rate of 0.5 Gyr^{-1}.

The ability of super spirals to survive under such a high merger rate depends on whether the mergers are major or minor, and also on the gas fraction (Hopkins et al. 2009). We find eight super spirals in major pairs ($\Delta g < 1.19$ mag) with separations <150 kpc (Table 9), that are likely to undergo transformative major mergers in the next Gyr. The remaining 35 mergers are minor pairs or double nuclei galaxies whose disks survived (including three S0/Sa galaxies). It is difficult to estimate the progenitor mass ratio for the double nuclei galaxies, but they must have either been minor mergers or unusually gas-rich mergers in order to retain or re-form their disks. If they are minor mergers, then the ratio of major to minor mergers is 0.18, roughly consistent with the 0.35–0.1 major/minor merger ratio predicted by Hopkins et al. (2010) for galaxies with $M_{\rm stars} = 10^{11-12}\ M_\odot$. It will be necessary to obtain H I and CO emission line measurements, or alternatively sub-mm dust continuum measurements, in order to determine the gas fractions of super spirals and its impact on their merger survivability.

8. Discussion: Super Spiral Growth and Destruction

Armed with an estimate of the merger rate (Section 7) and SSFRs (Section 3), measured at a median redshift of $z = 0.22$, we can predict the space densities and masses in stars of super spiral progenitors at intermediate redshift ($z = 1.0$). Over that redshift interval (a period of 5.2 Gyr), both rates should increase by roughly a factor of 2, according the model of Hopkins et al. (2010), yielding an average merger rate of 1.3 Gyr^{-1} and $1/{\rm SSFR} = 20.6$ Gyr along the ridge line of the SFMS. At this merger rate, super spirals will on average undergo 5.5 minor mergers with $\mu \sim 0.1$ and 1.2 major mergers with $\mu > 0.3$ between $z = 1.0$ and $z = 0.22$. Roughly 70% of super spirals will be transformed into giant ellipticals or super lenticulars by major mergers over this redshift interval, reducing the comoving space density of super spirals by a factor of 3.3 and increasing the comoving space density of giant ellipticals by a factor of 1.3.

Typical super spiral progenitors will increase their disk mass in stars by 33% from $z = 1.0$ to the present via steady, in situ star formation. Super spirals that do not experience a major merger in this time will increase their mass in stars by another 69% from direct acquisition of stars through minor mergers, most of which will be incorporated into their halos and thick disks. Gas-rich minor mergers will also add gas to super spiral disks, which may be transformed into additional mass in stars via merger-induced starbursts. Assuming a gas fraction of 0.5 for the secondary galaxy, and that half of this gas is converted into stars, super spiral mass in stars will grow by an additional 35% from merger-induced starbursts, with most of this mass incorporated into the disk. Together with steady in situ star formation, this yields a combined 68% gain in disk mass in stars.

From this model, we predict that 70% of super spirals were destroyed by major mergers from $z = 1.0$ to $z = 0.2$ and transformed into giant ellipticals or super lenticulars. The remaining 30% that survived through this time period increased their total mass in stars by a factor of 2.4, with half going to the disk and half going to the halo, while maintaining a relatively low B/T. The answer to the question of how super spirals survive is twofold. First, those that did survive are a factor of two less massive than giant ellipticals and therefore reside in regions that are on average a factor of two less dense, resulting in a lower overall merger rate. Second, their large masses protect them from mergers, such that 82% of all super spiral mergers at $z = 0.2$ are minor mergers that do not destroy their disks.

9. Conclusions

We present a catalog of 84 SDSS super spirals, 15 super lenticulars, 14 post-mergers, and 1400 giant ellipticals, selected for r-band luminosity $L_r > 8L^*$ and redshift $z < 0.3$. These galaxies represent the most massive galaxies in their redshift range, with masses in stars of $10^{11.3}$–$10^{12.3}\ M_\odot$. Super spirals are characterized by very large, high-mass, high-surface-brightness, actively star-forming disks that fall on or below the SFMS of galaxies. Super lenticulars have low SSFRs, particularly red optical colors, and no discernible spiral arms. Super post-mergers may be the product of super spiral major mergers, caught during the quenching phase, before they have completely ceased star formation.

The location of super spirals in *WISE*–SDSS color space shows that their star-forming disks contain a mix of young and old stellar populations. Their *WISE* [4.6]–[12] colors are relatively blue compared to less-massive spirals because they have accumulated large masses of old stars in their disks, resulting from early formation in some of the most-massive dark matter halos. Super spiral disks are red on the inside and blue on the outside, consistent with ongoing growth and inside-out formation by accretion of cold gas and minor mergers. Super spirals must form stars at a high rate throughout their lifetimes in order to grow their massive, gigantic disks and maintain their blue integrated colors.

Super disk galaxies are primarily found in moderate density environments, with on average half as many companions within 150 kpc, compared to giant ellipticals. For the 28% found in galaxy clusters, they are located at the cluster outskirts, with high relative velocities (~2000 km s^{-1}), consistent with the morphology–density relation. Star formation quenching is not an inevitable conclusion for the most-massive spiral galaxies, provided that they do not live at the dense centers of the largest galaxy clusters. Super spirals that do suffer major mergers may be transformed into super lenticulars or giant elliptical galaxies, providing a possible pathway to generate isolated giant elliptical galaxies outside of galaxy clusters.

A large percentage (41%) of super disk galaxies are involved in ongoing mergers or interactions with other galaxies. We suggest that some super spirals survive because most mergers are minor mergers for such massive galaxies. Super spirals have low bulge/total luminosity ratios, also consistent with disk building by cold gas accretion and bulge construction by minor mergers. While a large reservoir of high-angular-momentum gas could also aid in preserving the structure of super spirals, it will require sensitive radio and sub-mm observations to establish whether or not this is actually the case.

Super spirals and super lenticulars are disk galaxy counterparts to the most-massive, giant elliptical galaxies. Star formation remains unquenched in most super spirals, in spite of their very large masses of old stellar populations. In fact, they appear to have survived through the ages in moderately dense

environs, by virtue of their large masses. Anticipating future studies, the extreme masses, luminosities, and sizes of super spirals will open new parameter space for testing galaxy scaling laws and theories of massive galaxy formation and evolution. The large ongoing merger fraction and variety of merger mass ratios and geometries present in super spiral systems also provide a unique opportunity to study the impact of mergers on massive spiral galaxy structure, star formation, and evolution.

We thank Katey Alatalo for insightful discussions regarding the properties of post-merger and post-starburst galaxies. This work was made possible by the NASA/IPAC Extragalactic Database and the NASA/IPAC Infrared Science Archive, which are both operated by the Jet Propulsion Laboratory, California Institute of Technology, under contract with the National Aeronautics and Space Administration. We thank Ben Chan, Marion Schmitz, and the rest of the NED team for useful discussions and their support of this work. This publication makes use of data from the *Galaxy Evolution Explorer* and the *Hubble Space Telescope*, retrieved from the Mikulski Archive for Space Telescopes (MAST). STScI is operated by the Association of Universities for Research in Astronomy, Inc., under NASA contract NAS5-26555. Support for MAST for non-*HST* data is provided by the NASA Office of Space Science via grant NNX09AF08G and by other grants and contracts. Funding for the Sloan Digital Sky Survey IV has been provided by the Alfred P. Sloan Foundation, the U.S. Department of Energy Office of Science, and the Participating Institutions. SDSS acknowledges support and resources from the Center for High-Performance Computing at the University of Utah. The SDSS website is www.sdss.org. SDSS is managed by the Astrophysical Research Consortium for the Participating Institutions of the SDSS Collaboration. This publication makes use of data products from the Two Micron All Sky Survey, which is a joint project of the University of Massachusetts and the Infrared Processing and Analysis Center/California Institute of Technology, funded by the National Aeronautics and Space Administration and the National Science Foundation. This publication makes use of data products from the *Wide-field Infrared Survey Explorer*, which is a joint project of the University of California, Los Angeles, and the Jet Propulsion Laboratory/California Institute of Technology, funded by the National Aeronautics and Space Administration.

Appendix

A.1. Catalog of the Most Optically Luminous Galaxies

The Ogle et al. Galaxy Catalog (OGC) is presented in this Appendix (Table 2), including catalog names, SDSS *r*-band magnitude, *K*-corrected *r*-band luminosity, redshift, morphology, and spectral type. Catalog sources that we reject based on photometric contamination, bad redshifts, and spatial overlap with foreground or background sources are presented in Tables 3–5. Derived physical properties are presented for super spirals, lenticulars, and post mergers in Table 6. We present images of super spirals, lenticulars, and post-mergers at a scale of 150 kpc on a side in Figures 11–13 and images of their larger (300 kpc × 300 kpc) environs in Figures 14 and 15. Non-spiral galaxies with SEDs dominated by AGNs or with significant contamination by stars are listed in Table 7. Super spiral and lenticular associations with galaxy clusters and groups are given in Table 8, including cluster names, redshifts, galaxy counts, and separation. Candidate super spiral and lenticular mergers and pair separations are found in Table 9.

A.2. Non-spiral AGNs and Quasi-stellar Object Hosts

There are 12 non-spiral galaxies with SEDs contaminated by bright type-1 AGNs or stellar objects that we excluded from our analysis (Table 7 and Figure 13). Among these are six spectroscpically verified quasi-stellar object (QSO) host galaxies (OGC 0239, 0302, 0377, 0889, 1239, and 1245) and three known BL Lac hosts (OGC 0615, 0962, and 1229), where the AGNs may contribute significantly to the *r*-band luminosity. There are another three galaxies accompanied by bright stellar objects (OGC 0307, 0469, and 0646) which may be either stars or QSOs, for which no SDSS spectra are available. We originally identified QSO host OGC 0302 as a super spiral (Ogle et al. 2016), but *HST* imaging shows it to be a disturbed, possibly post-merger galaxy rather than a spiral galaxy (Figure 16).

A.3. Gravitational Lenses

Galaxy-scale gravitational lenses are potential contaminants to our sample that may artificially boost the *r*-band flux or present arc-like features that can be mistaken for spiral arms (Figure 16). For example, the giant elliptical galaxy OGC 0203 (2MASX J11125450 +1326093 in A1201) is a known gravitational lens, with a lens arc projected $2\farcs0$ from its center (Edge et al. 2003). We initially identified the previously unknown gravitational lens OGC 0200 (2MASX J08355126 +3926220) as a super spiral, but an existing *HST* image shows multiple lens arcs that masquerade as faint spiral arms in the lower-resolution SDSS images. Finally we identify the brightest cluster galaxy OGC 1565 (2MASX J21531028+1154551, $z = 0.289$) as a gravitational lens candidate and possible Einstein ring by the unusual red ring that encircles it (Figure 16).

Table 2
The Ogle et al. Galaxy Catalog (OGC)

OGC	NED Name	L_r[a]	r (mag)[b]	z (NED)[c]	Morph.[d]
0021	2MASX J12220526+4518109	19.8	16.26	0.264357	E
0022	B3 1715+425	19.5	15.34	0.182900	E
0023	SDSS J215541.97+123128.5	19.1	15.68	0.193000	E
…					
0078	2MASX J02295551+0104361	13.3	16.53	0.245472	E
…					
1606	SDSS J121644.34+122450.5	8.0	17.22	0.257144	SS
1607	SDSS J130454.84+100011.6	8.0	17.19	0.255875	E
1608	SDSS J040422.91−054134.9	8.0	17.27	0.250635	SS
1609	2MASX J12071504+1713488	8.0	16.87	0.221788	E
1610	2MASX J08302311+4744471	8.0	17.10	0.243735	E
1611	2MASX J00380781−0109365	8.0	16.65	0.208695	S0
1662[e]	SDSS J085123.17−002148.7	7.9	17.59	0.295481	Epec

Notes.
[a] SDSS r-band luminosity, K-corrected, and divided by $L^* = 5.41 \times 10^{43}$ erg s^{-1}.
[b] SDSS r-band CModel magnitude.
[c] NED preferred redshift, primarily from SDSS DR6.
[d] Galaxy morphology: G = unclassified galaxy, E = elliptical, Epec = peculiar elliptical, S0 = super lenticular, S = spiral, SS = super spiral.
[e] The starburst galaxy OGC 1662 falls below the $8.0L^*$ cutoff of the sample (horizontal line), but we include it in this table, Table 6, and Figure 13 to point out its unusual properties.

(This table is available in its entirety in machine-readable form.)

Table 3
Luminous Galaxy Rejects: Inaccurate Photometry

OGC	NED Name	Notes
0001	SDSS J101736.97+305101.6	glare
0003	SDSS J091428.98+184250.9	glare
0004	SDSS J102825.27+154757.2	glare
…		
1418	2MASX J14352497−0105084	bright star
1425	2MASX J10240215+2534587	glare
1585	2MASX J09095768+5731219	bright star

(This table is available in its entirety in machine-readable form.)

Table 4
Luminous Galaxy Rejects: Incorrect Redshifts

OGC	NED Name	z (NED)	References (1)	Adopted z	References (2)
0005	2MASX J14342221+0706510	0.254000	RK12	…	…
0006	CGCG 045-047	0.192300	HT10	…	…
0008	2MASX J13041968+4214150	0.201700	HT10	0.03611	DR12
0011	UGC 08569	0.140657	FK99	0.02303	DR12
0012	2MASX J16521103+2344396	0.178900	HT10	0.03471	DR12
0013	2MASX J11064145+3435219	0.158800	HT10	…	…
0014	LCSB S2225P	0.222100	RR05	…	…
0015	MCG +08-24-006	0.149600	HT10	…	…
0019	SBS 0957+569	0.147600	HT10	0.01368	DR12
0020	SDSS J082143.27+011423.2	0.295711	GS09	…	…
0024	CGCG 208-020	0.132400	HT10	0.02457	DR12
0026	2MASX J15032011+0856496	0.168000	LS10	…	…
0030	2MASX J01132663+1520072	0.203174	CB09	0.04232	DR12
0036	2MASX J01122497+1538371	0.217106	CB09	0.04423	DR12
0038	2MASX J14153929+2313477	0.252000	BG06	0.06369	DR12
0045	2MASX J16064936+3202464	0.135400	HT10	0.11550	DR12
0052	VCC 0838	0.295417	CG01	…	…
0056	KUG 1320+255	0.143843	RG01	0.03322	DR12
0069	2MASX J09075107+4401533	0.114500	HT10	0.04878	DR12

Table 4
(Continued)

OGC	NED Name	z (NED)	References (1)	Adopted z	References (2)
0102	SDSS J135128.05+091559.7	0.294330	DR6	0.06062	DR12
0172	2MASX J21472854-0738031	0.148299	6dF	0.05971	DR12
1035	SDSS J141655.53+234018.2	0.281682	DR13	0.11548	DR12
1274	UGC 10782	0.086000	VC04	0.036	VC04
1343	2MASX J12110100+3048346	0.192703	DR6	0.12861	DR12

References. DR6, 12, 13 = SDSS Data Release 6, 12, 13, 6dF = 6dF Galaxy Survey, BG06 = Barkhouse et al. (2006), CB09 = Cava et al. (2009), CG01 = Conselice et al. (2001), FK99 = Falco et al. (1999), GS09 = Guzzo et al. (2009), HT10 = Hernandez-Toledo et al. (2010), LS10 = Lin et al. (2010), RG01 = Rines et al. (2001), RK12 = Rykoff et al. (2012), RR05 = Rowan-Robinson et al. (2005), VC04 = Veron-Cetty et al. (2004).

Table 5
Luminous Galaxy Rejects: Overlapping Objects

OGC	Object 1 (NED)	Type 1	Object2	Type 2
0002	SDSS J104819.41+123745.8	compact	NGC 3384	E
0010	SDSS J104248.72+132710.7	compact	UGC 05832	Irr
0025	SDSS J141309.29+083707.2	compact	VV 299a	Irr
0031	2MASX J12494045+2546186	compact	KUG 1247+260	dE
0048	2MASX J07543650+3905307	dE?	no name	compact
0059	2MASX J08540011+5751327	E	no name	S, edge-on
0146	SDSS J092209.32+335057.4	compact	UGC 04974	E
0191	VIII Zw 125 NOTES02	QSO	SDSS J110717.65+080435.3	E
0379	KUG 0907+332	E	SDSS J091031.83+330327.9	Irr
0706	SDSS J142418.44+293238.4	E	SDSS J142418.71+293232.9	S
1176	SDSS J144700.16+011504.9	F9 star ($cz = 9$ km s^{-1})	no name	G
1322	SDSS J014503.26−001800.0	S	UGC 01225 NED02	Irr
1360	SDSS J123433.28+181154.8	E	NGC 4539	S0
1406	2MASX J11523751+1527539	E	SDSS J115237.63+152759.1	S
1497	SDSS J020707.48−082726.0	compact	GALEXASC J020707.37−082723.5	Irr
1565	2MASX J21531028+1154551	GLens candidate	no name	lensed galaxy

Note. Galaxy morphology: compact = star or compact galaxy, G = unclassified galaxy, S = spiral, S0 = lenticular, E = elliptical, dE = dwarf elliptical, Irr = irregular galaxy, QSO = quasi-stellar object, GLens = gravitational lens.

Table 6
OGC Super Spirals, Lenticulars, and Post-mergers

OGC	NED Name	z(SDSS)[a]	L_r[b]	D[c]	log M_{stars}[d]	log SFR[e]	Morph.[f]	Spect.[g]
0065	2MASX J10301576−0106068	0.28228	13.9	81	11.65	1.21	bar	
0139	2MASX J16394598+4609058	0.24713	12.0	134	11.71	1.31	⋯	Hα
0170	2MASX J10100707+3253295	0.28990	11.6	87	11.65	1.08	bar	Hα
0179	SDSS J213701.13−064447.0	0.29065	11.5	76	11.88	0.34	⋯	⋯
0217	2MASX J13275756+3345291	0.24892	11.2	69	11.52	1.50	bar	Hα, sb
0222	2MASX J12220815+4844557	0.29861	11.1	95	11.78	0.44	⋯	⋯
0256	2MASX J11593546+1257080	0.26353	10.9	87	11.56	0.90	⋯	Hα
0290	2MASX J12343099+5156295	0.29592	10.6	62	11.55	1.26	⋯	Sey1
0293	2MASX J13044128+6635345	0.28862	10.6	77	11.74	0.69	⋯	Hα
0299	2MASX J09094480+2226078	0.28539	10.5	83	11.84	0.65	⋯	⋯
0306	SDSS J122100.48+482729.1	0.29966	10.5	75	11.72	0.79	⋯	⋯
0345	2MASX J09260805+2405242	0.22239	10.3	81	11.72	1.17	⋯	Hα
0388	2MASX J17340613+6029190	0.27596	10.1	64	11.57	0.84	⋯	⋯
0441	SDSS J095727.02+083501.7	0.25652	9.9	88	⋯	0.81	⋯	⋯
0454	2MASXi J1003568+382901	0.25860	9.9	56	11.68	1.28	⋯	Hα, sb
0516	2MASX J14475296+1447030	0.22069	9.7	95	11.65	0.89	⋯	LINER
0543	2MASX J09470010+2540462	0.10904	9.6	99	11.65	1.05	bar	Sey1
0574	SDSS J121148.70+662514.4	0.23789	9.5	63	11.75	0.96	⋯	Hα
0586	2MASX J11535621+4923562	0.16673	9.5	90	11.63	1.27	⋯	Sey2
0595	2MASX J07550424+1353261	0.22264	9.5	77	11.53	0.96	bar	⋯
0612	SDSS J093540.34+565323.8	0.29636	9.4	92	11.98	⋯	bar	
0623	2MASX J09011007+2454570	0.25232	9.4	74	11.55	1.03	⋯	Sey1
0637	2MASX J15575566+4322473	0.20641	9.3	80	11.60	0.72	⋯	Hα

Table 6
(Continued)

OGC	NED Name	z(SDSS)[a]	L_r[b]	D[c]	log M_{stars}[d]	log SFR[e]	Morph.[f]	Spect.[g]
0696	SDSS J102154.85+072415.5	0.29061	9.2	70	⋯	0.90	⋯	Hα
0704	2MASX J03460305+0100064	0.18605	9.2	83	11.46	0.91	⋯	⋯
0713	2MASX J08265512+1811476	0.26545	9.2	82	11.64	0.93	bar	⋯
0749	2MASX J15591044+3826290	0.29073	9.1	70	11.56	0.98	bar	Sey1
0753	2MASX J08022926+2325161	0.27152	9.1	66	11.35	0.98	⋯	Hα
0755	SDSS J113800.88+521303.9	0.29593	9.1	64	11.59	0.79	⋯	⋯
0789	2MASX J08542169+0449308	0.15679	9.0	86	11.58	1.13	bar	Hα
0799	2MASX J10472505+2309174	0.18256	9.0	72	11.65	1.01	bar	
0800	2MASX J11191739+1419465	0.14377	9.0	71	11.55	0.98	⋯	⋯
0804	SDSS J135546.07+025455.8	0.23884	9.0	84	⋯	0.77		
0830	SDSS J141754.96+270434.4	0.15753	9.0	69	11.69	0.90	⋯	⋯
0909	2MASX J14381016+5030122	0.24665	8.8	66	11.53	0.32	⋯	⋯
0926	2MASX J10304263+0418219	0.16092	8.8	70	11.66	1.36	⋯	Hα
0928	2MASX J12374668+4812273	0.27245	8.8	66	11.46	1.08	⋯	Hα
0968	2MASX J09312816+4424163	0.21940	8.7	65	11.50	1.29	bar	Sey2, not a starburst
0975	2MASX J11410001+3848078	0.26770	8.7	72	11.54	1.08	⋯	⋯
0983	SDSS J153618.97+452246.8	0.23618	8.7	80	11.43	0.71	⋯	⋯
0984	SDSS J133737.88+494015.6	0.27233	8.7	73	11.74	0.35	⋯	Hα
0995	2MASX J14440406+2029072	0.24820	8.7	76	11.83	0.31	⋯	Hα
1023	2MASX J09254889+0745051	0.17227	8.6	68	11.62	0.85	⋯	Hα
1046	2MASX J09362208+3906291	0.28293	8.6	70	11.42	0.85	⋯	⋯
1088	SDSS J140138.37+263527.6	0.28396	8.5	78	⋯	0.90		Hα
1094	SDSS J163357.99+172839.5	0.26691	8.5	77	⋯	1.08		Hα
1107	2MASX J12072497−0150416	0.20957	8.5	69	11.46	0.91	bar	⋯
1166	2MASX J22295446−0921345	0.27954	8.4	57	11.49	0.46	⋯	
1182	2MASX J00495939−0853413	0.12181	8.4	66	11.84	0.82	⋯	Hα
1196	SDSS J154950.91+234444.1	0.26208	8.4	69	⋯	0.99	⋯	Hα
1250	2MASX J12321515+1021195	0.16588	8.3	71	11.42	0.88	⋯	⋯
1268	2MASX J12005393+4800076	0.27841	8.3	63	11.46	1.04	⋯	Hα
1273	2MASX J07380615+2823592	0.23091	8.3	77	11.46	0.97	bar	⋯
1287	2MASX J07404205+4332412	0.17828	8.3	69	11.62	0.90	⋯	Hα
1304	2MASX J16014061+2718161	0.16440	8.3	82	11.80	1.33	⋯	Hα
1312	SDSS J143447.86+020228.6	0.27991	8.2	75	11.68	1.26	⋯	Hα, not a starburst
1323	SDSS J112928.74+025549.9	0.23960	8.2	70	11.70	0.94	bar	⋯
1329	2MASX J16273931+3002239	0.25990	8.2	86	11.75	0.48	⋯	Hα
1337	SDSS J093921.25+260709.8	0.27487	8.2	56	11.70	0.68	⋯	Hα
1352	SDSS J101603.97+303747.9	0.25191	8.2	69	12.00	⋯		Hα
1375	2MASX J00155012−1002427	0.17601	8.2	68	11.47	0.75	⋯	Hα
1379	2MASX J09373465+1036552	0.17946	8.2	90	11.58	1.04	bar	Hα
1395	2MASX J13103930+2235023	0.23123	8.1	66	11.53	0.86	⋯	⋯
1409	SDSS J151721.02+603302.6	0.28232	8.1	70	11.62	0.79	⋯	Hα
1420	2MASX J13475962+3227100	0.22306	8.1	88	11.50	0.93	⋯	⋯
1423	SDSS J215250.41+122159.2	0.27310	8.1	61	⋯	0.90		Hα
1428	2MASX J11162790+3813476	0.23350	8.1	77	11.34	0.89	⋯	⋯
1450	SDSS J132743.82−031323.1	0.29502	8.1	64	⋯	0.91		Hα
1457	2MASX J09381666+1044508	0.23897	8.1	72	11.37	1.26	⋯	Hα, sb
1464	2MASX J10041606+2958441	0.29844	8.1	57	11.47	1.39	⋯	Hα, sb
1500	2MASX J10095635+2611324	0.24089	8.1	64	11.44	0.96	⋯	Hα
1501	2MASX J09334777+2114362	0.17219	8.1	64	11.62	1.43	⋯	QSO, not a starburst
1512	SDSS J122944.64+272306.3	0.27573	8.0	101	11.48	0.89	⋯	Hα, not a starburst
1514	SDSS J080317.08+325932.6	0.24848	8.0	55	11.89	0.24	⋯	⋯
1520	2MASX J12354859+3919078	0.23706	8.0	63	11.64	1.46	⋯	Hα, sb
1544	2MASX J14472834+5908314	0.24551	8.0	68	11.58	0.80	bar	Hα
1546	2MASX J13435549+2440484	0.13725	8.0	66	11.59	0.66	⋯	Hα
1549	2MASX J08464747+0446053	0.24145	8.0	76	12.01	⋯	⋯	⋯
1554	2MASX J13422833+1157345	0.27873	8.0	57	11.53	0.94	⋯	Hα
1559	CGCG 122-067	0.08902	8.0	81	11.71	0.93		Hα
1562	SDSS J163202.04+464545.7	0.29491	8.0	67	11.64	0.61	⋯	Hα
1600	SDSS J115155.92+104634.7	0.28305	8.0	67	11.63	0.22	⋯	Hα
1606	SDSS J121644.34+122450.5	0.25694	8.0	78	⋯	0.95	bar	Sey1
1608	SDSS J040422.91−054134.9	0.25055	8.0	80	11.51	0.78	⋯	Hα
0044	2MASX J14072225+1352512	0.29372	15.1	85	11.92	0.47	S0/Sa	⋯
0073	2MASX J10405643−0103584	0.25024	13.4	82	11.81	0.49	S0/Sa	⋯

Table 6
(Continued)

OGC	NED Name	z(SDSS)[a]	L_r[b]	D[c]	log M_{stars}[d]	log SFR[e]	Morph.[f]	Spect.[g]
0265	SDSS J115052.98+460448.1	0.28946	10.8	88	11.80	0.10	S0/Sa	⋯
0280	2MASX J09572689+4918571	0.24144	10.7	106	11.81	0.60	S0/Sa	⋯
0425	2MASX J21160443−0702228	0.19082	10.0	77	11.85	0.60	S0/Sa	Hα
0581	2MASX J13423113+0021440	0.24342	9.5	142	11.80	0.64	S0/Sa	⋯
1002	2MASX J10535662+5909155	0.19896	8.7	84	11.69	0.76	S0/Sa	Hα
1220	2MASX J08164326+4702216	0.29529	8.3	62	11.55	0.63	S0/Sa	Hα
1270	SDSS J125157.99+305422.3	0.23065	8.3	78	11.77	0.48	S0/Sa	Hα
1291	SDSS J090317.22−000758.9	0.29726	8.3	72	11.77	0.33	S0/Sa	Hα
1381	2MASX J08093749+2316385	0.27291	8.2	81	11.65	0.33	S0/Sa	⋯
1386	2MASX J13382172+0929423	0.24302	8.2	92	11.59	0.68	S0/Sa	⋯
1526	2MASX J11414166+0223211	0.23354	8.0	89	11.58	0.39	S0/Sa	Hα
1535	2MASX J11160517+3303477	0.20616	8.0	94	11.65	0.36	S0/Sa	⋯
1611	2MASX J00380781−0109365	0.20828	8.0	84	11.70	0.74	S0/Sa	Hα
0247	SDSS J081953.52+041409.2	0.296625	10.9	43	11.56	0.90	Pec	K + A + Sey1
0331	SDSS J091318.25+492556.3	0.296414	10.4	43	11.52	0.80	Pec	K + A + Sey1
0624	2MASX J13245634+6219585	0.237397	9.4	69	11.64	1.06	Pec	K + A ? + Sey1
0707	2MASX J11304267+1538467	0.298136	9.2	61	11.50	0.60	Pec	K + A
0783	SDSS J102629.10+094519.7	0.262280	9.0	72	11.69	0.82	Pec	K + A
0892	SDSS J095543.25+111715.9	0.299029	8.8	66	11.70	0.18	Pec	Hα
0902	2MASX J23591456+1351308	0.247131	8.8	55	11.56	1.34	Pec	Hα, sb
0973	2MASX J13412783+2851280	0.294948	8.7	47	11.59	1.03	Pec	K + A + Hα
1056	SDSS J120050.60−012755.6	0.267160	8.6	117	⋯	0.57	Pec	
1058	2MASX J12383963+6413430	0.265032	8.6	82	11.57	1.21	Pec	Hα, sb
1174	2MASX J11310763+0224271	0.257493	8.4	65	11.50	0.88	Pec	Hα
1377	SDSS J134719.23+114915.1	0.279850	8.2	66	11.46	0.77	Pec	K + A + Sey2
1413	MCG +09-25-047	0.244470	8.1	67	11.85	<1.90	Pec	K + A + Sey2
1490	2MASX J08164043+3340182	0.238297	8.1	58	11.34	0.88	Pec	K + A + [N II]
1662	SDSS J085123.17−002148.7	0.295481	7.9	72	⋯	1.19	Pec	Hα, sb

Notes.
[a] SDSS DR9 redshift.
[b] L/L^* (Sloan r band).
[c] Isophotal diameter (kpc) at $r = 25.0$ mag arcsec^{-2}.
[d] log of mass in stars ($M_\odot$).
[e] log of star formation rate ($M_\odot$ yr^{-1}).
[f] Morphology. Lenticular galaxies are denoted S0/Sa. Galaxies with stellar bars are indicated as such. Horizontal lines in the table separate super spirals, super lenticulars, and super post-mergers.
[g] Notes on SDSS spectroscopy. Hα indicates detection of that line in the SDSS spectrum. AGNs are marked as Seyfert 1 (Sey1), Seyfert 2 (Sey2), LINER, or QSO. Galaxies with nuclear starbursts are marked sb. K + A indicates a post-starburst spectrum dominated by A stars.

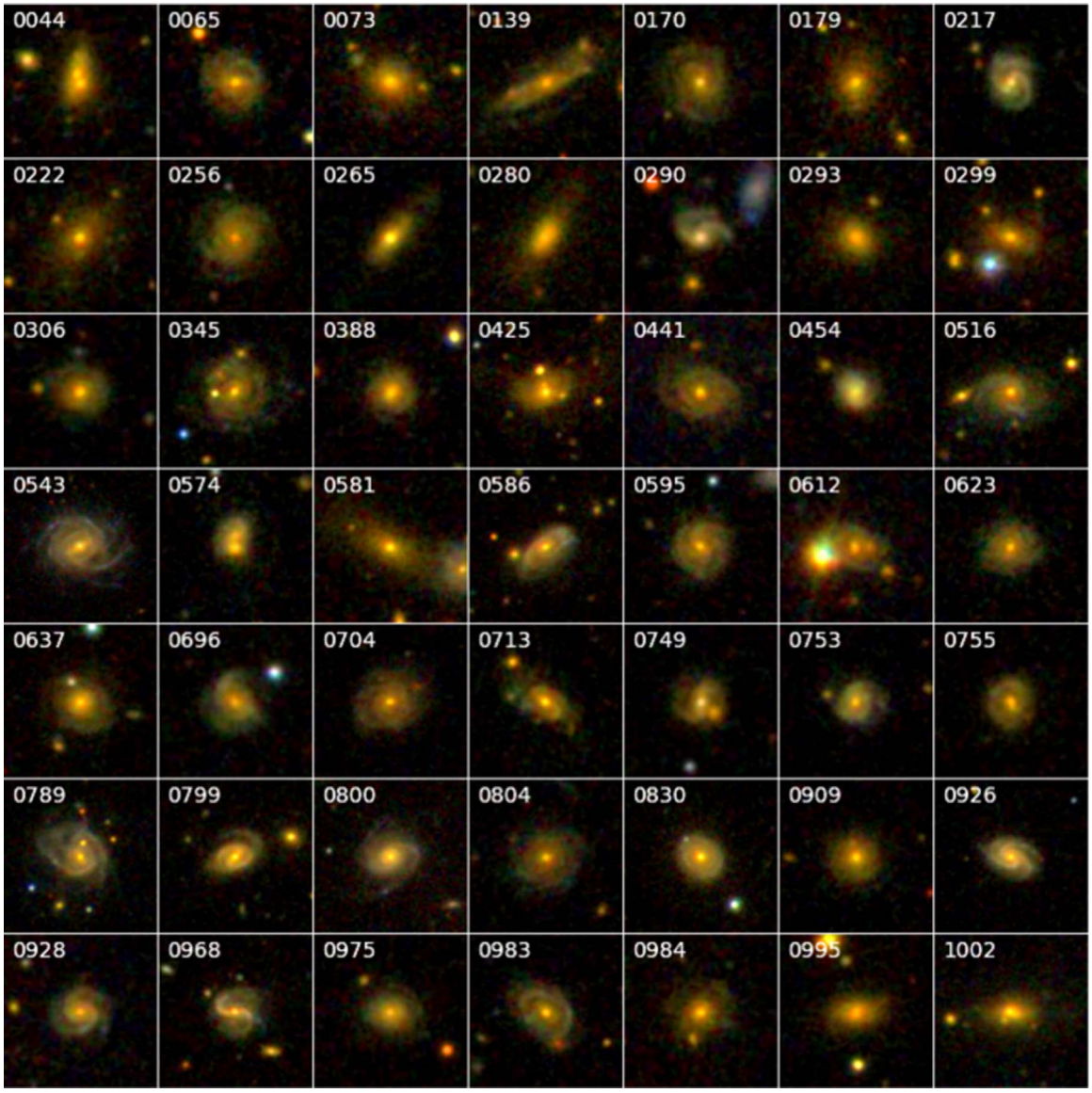

Figure 11. SDSS images of super spiral and super lenticular galaxies OGC 0044–1002, ordered by decreasing *r*-band luminosity. Each image is 150 kpc on a side.

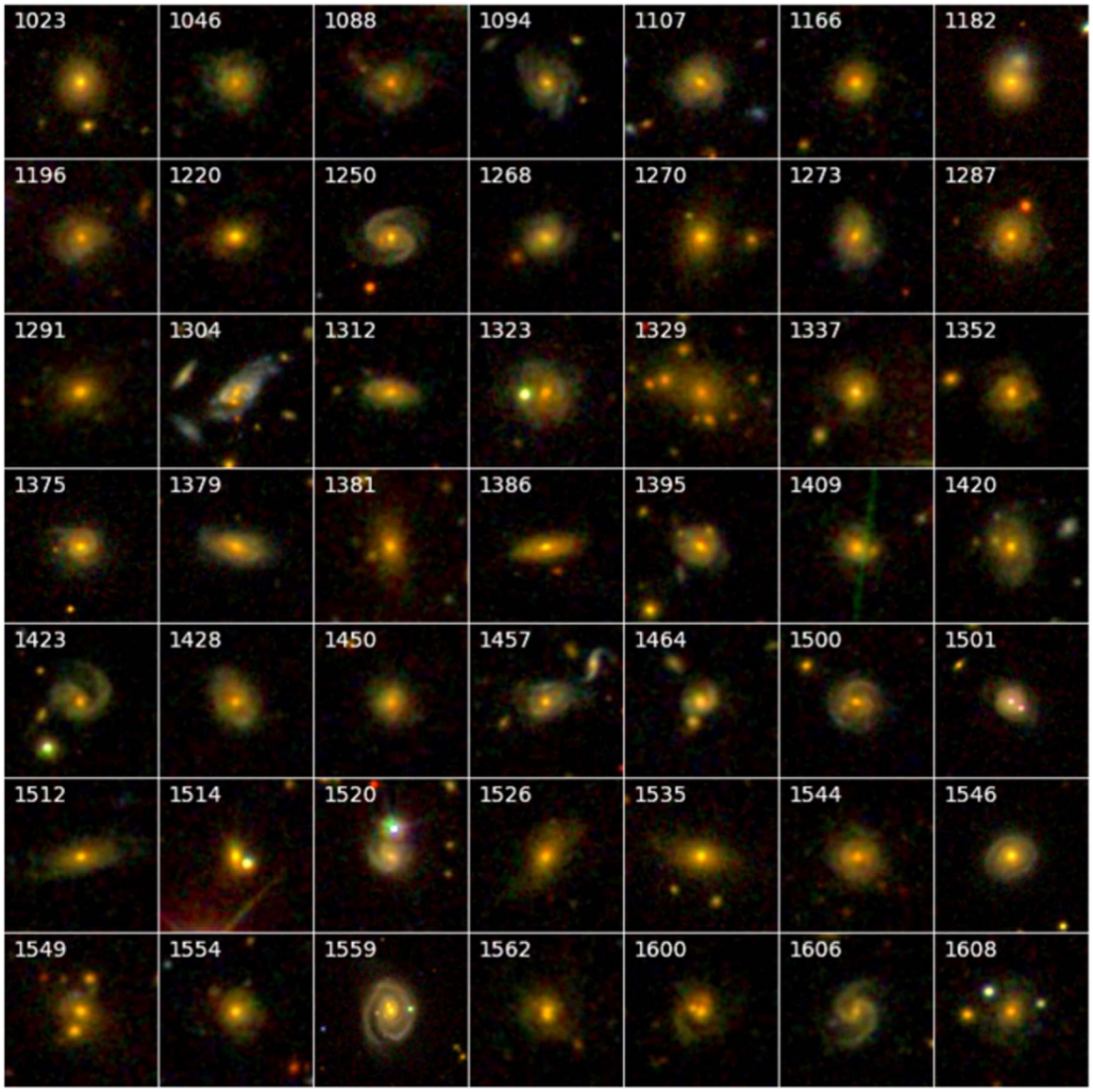

Figure 12. SDSS images of super spiral and super lenticular galaxies OGC 1023–1608, ordered by decreasing *r*-band luminosity. Each image is 150 kpc on a side.

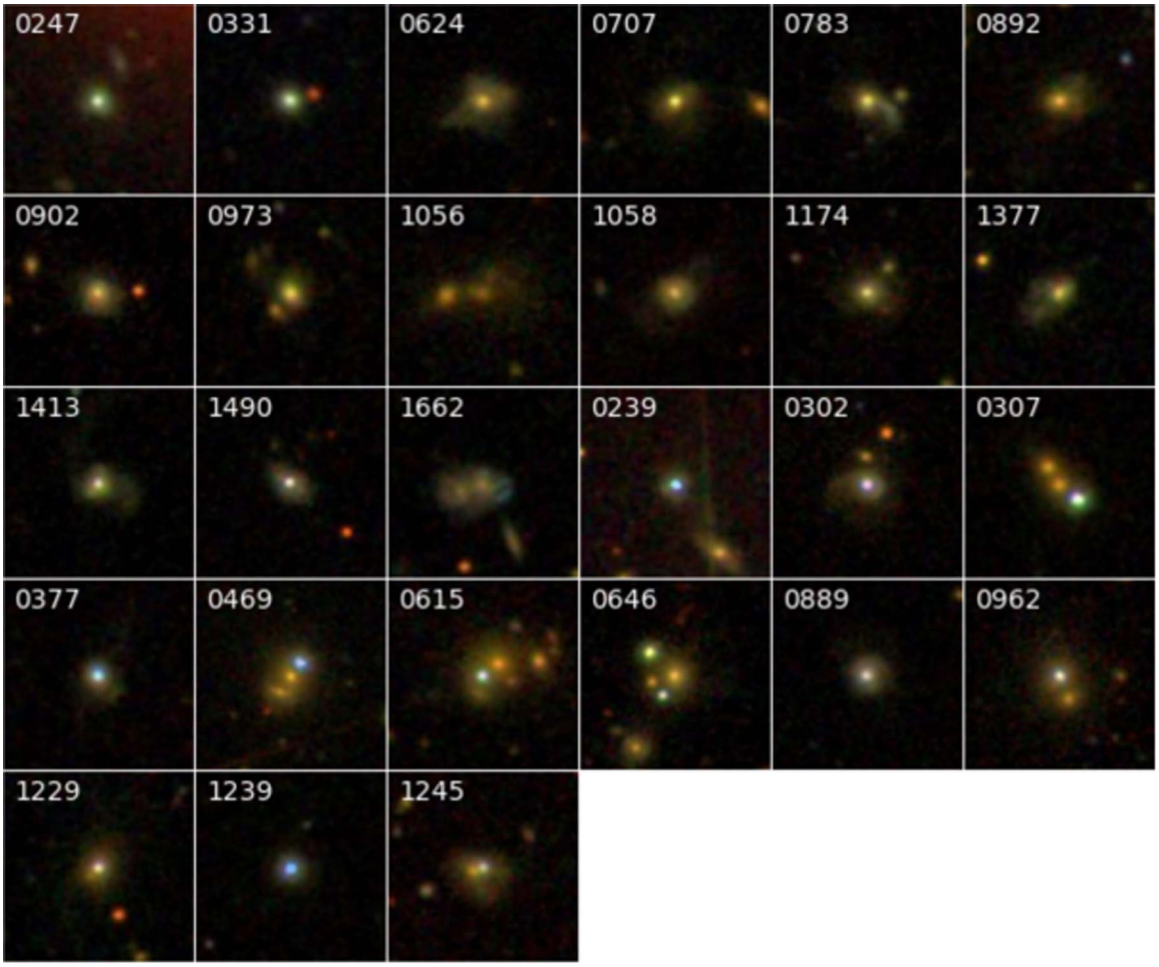

Figure 13. SDSS images (150 kpc on a side) of super post-mergers (OGC 0247–1662), followed by non-spiral quasi-stellar objects, or BL Lac hosts, or galaxies with stellar companions (OGC 0239–1245).

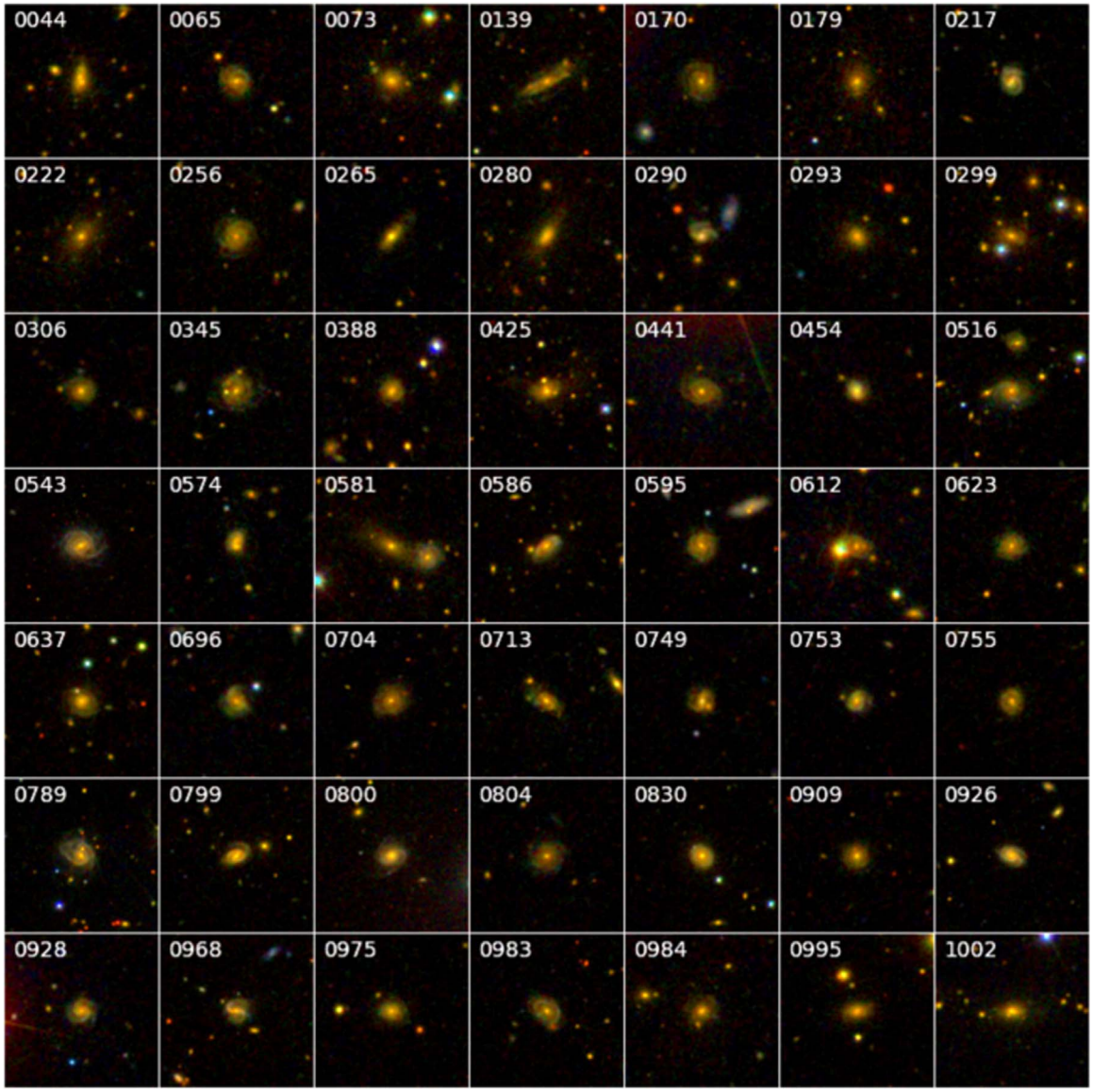

Figure 14. SDSS images of the environs of super spiral and super lenticular galaxies OGC 0044–1002, ordered by decreasing *r*-band luminosity. Each field of view is 300 kpc on a side.

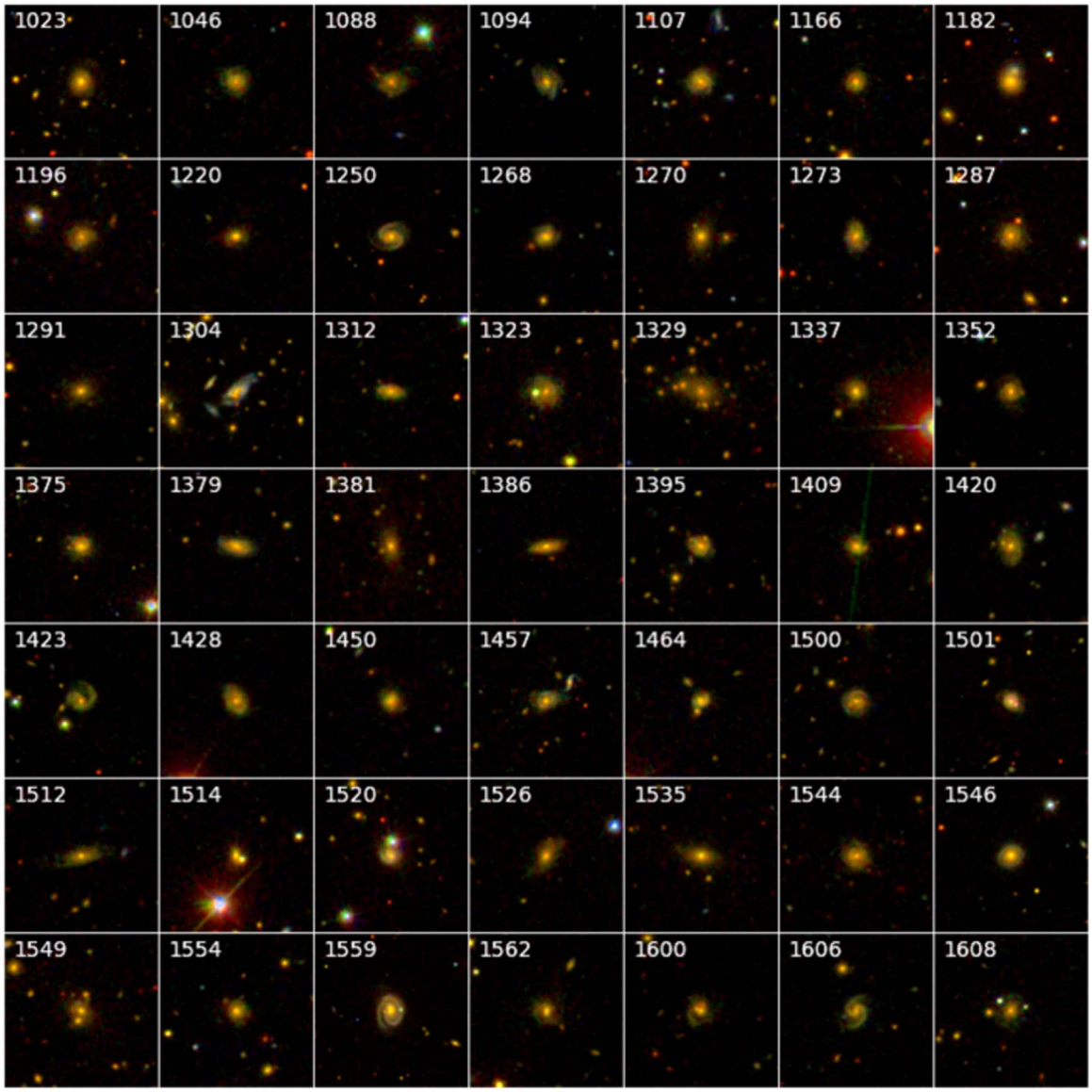

Figure 15. SDSS images of the environs of super spiral and super lenticular galaxies OGC 1023–1608, ordered by decreasing *r*-band luminosity. Each field of view is 300 kpc on a side.

Table 7
OGC AGN-dominated

OGC	NED Name	Other Name	Image	Spectrum
0239	2MASX J11552373+1507564	⋯	AGN host	QSO
0302	2MASX J15430777+1937522	⋯	AGN host	QSO
0307	SDSS J143335.34+242039.2	⋯	2E + star?	⋯
0377	2MASSi J2342593+134750	⋯	AGN host	QSO
0469	SDSS J150022.77+220027.3	NVSS J150022+220027	2G + star?	⋯
0615	2MASXi J0837247+145819	ABELL 0689:[REE2012] BCG	AGN host	BLLac
0646	2MASX J21193928+1039326	⋯	2E + 2 stars?	⋯
0889	2MASX J08250928+2634381	⋯	AGN host	QSO
0962	SDSS J141756.67+254326.2	⋯	AGN host	BL Lac
1229	2MASX J08574977+0135301	⋯	AGN host	BL Lac
1239	SDSS J145608.63+380038.5	⋯	AGN host	QSO
1245	2MASX J02354663−0742506	⋯	AGN host	QSO

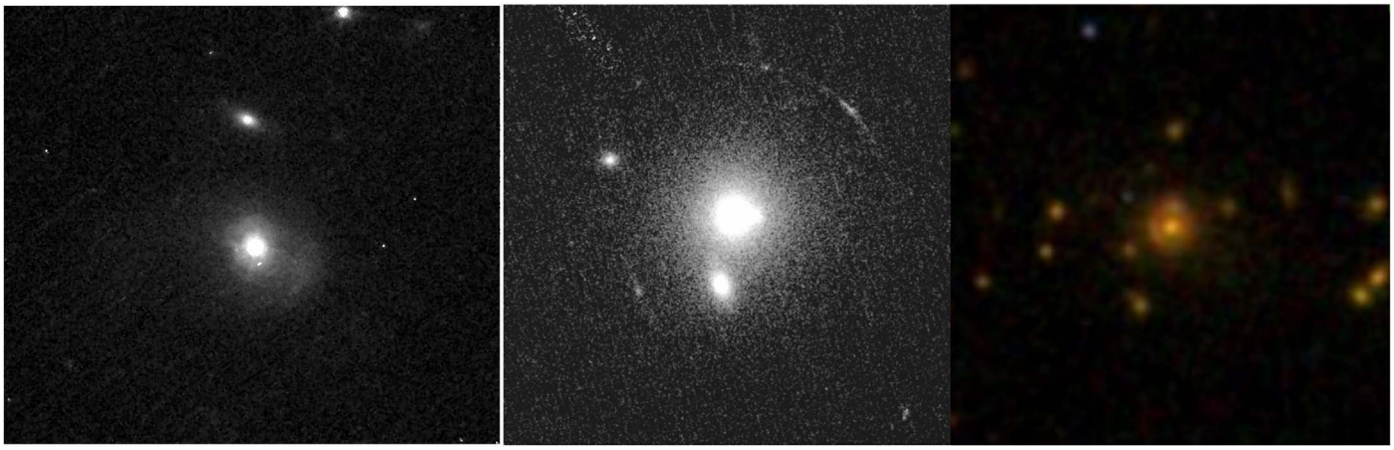

Figure 16. Left: *HST* WFPC2 F814W image of ex-super spiral OGC 0302, showing that it is a disturbed, non-spiral quasar host. The field of view is 24 × 21 arcsec (88 × 77 kpc). Center: elliptical galaxy and newly identified gravitational lens OGC 0200 (2MASX J08355126+3926220) imaged by *HST* ACS/HRC in the F775W filter (Proposal ID 10199). We initially classified this as a super spiral, mistaking the lens arcs for spiral arms. The field of view is 14 × 14 arcsec (56 × 56 kpc). Right: newly identified gravitational lens candidate OGC 1565 (2MASX J21531028+1154551). The field of view is 50 × 50 arcsec (217 × 217 kpc).

Table 8
Super Spiral and Lenticular Cluster and Group Associations

OGC	NED Name	Redshift	N1[a]	N10[b]	Cluster Name	Type	Redshift	ztype[c]	Sep(′)[d]
0044	2MASX J14072225+1352512	0.293596	1	23	GMBCG J211.84274+13.88070	GClstr	0.280850	PHOT	0.000
0073	2MASX J10405643−0103584	0.250303	1	13	SDSS CE J160.241898−01.069106	GClstr	0.254019	EST	0.013
0170	2MASX J10100707+3253295	0.289913	2	38	GMBCG J152.52936+32.89139	GClstr	0.319000	PHOT	0.001
0179	SDSS J213701.13−064447.0	0.290697	1	8	SDSSCGB 18956	GGroup	0.291000	SPEC	0.054
0280	2MASX J09572689+4918571	0.241492	5	26	MaxBCG J149.36205+49.31591	GClstr	0.237650	PHOT	0.000
0293	2MASX J13044128+6635345	0.288630	1	4	MaxBCG J196.17181+66.59301	GClstr	0.226850	PHOT	0.000
0299	2MASX J09094480+2226078	0.285386	2	17	GMBCG J137.43670+22.43538	GClstr	0.303000	PHOT	0.000
0345	2MASX J09260805+2405242	0.222451	1	36	WHL J092608.1+240524	GClstr	0.178000	PHOT	0.000
0388	2MASX J17340613+6029190	0.275807	1	2	SDSSCGB 59704	GGroup	0.276000	SPEC	0.450
0516	2MASX J14475296+1447030	0.220592	1	33	ABELL 1971	GClstr	0.208600	SPEC	1.298
					MaxBCG J221.98726+14.75906	GClstr	0.216050	PHOT	1.775
					WHL J144756.9+144532	GClstr	0.203600	PHOT	1.778
0581	2MASX J13423113+0021440	0.243520	1	47	SDSSCG 110	GGroup	0.243400	SPEC	0.439
					SDSS CE J205.645691+00.368013	GClstr	0.231327	EST	1.031
0586	2MASX J11535621+4923562	0.166892	3	70	OGC 0586 CLUSTER	GClstr	0.166187	SPEC	0.000
0612	SDSS J093540.34+565323.8	0.296393	1	21	ZwCl 0932.1+5708	GClstr	⋯	⋯	1.186
0637	2MASX J15575566+4322473	0.206452	1	18	MaxBCG J239.48210+43.37988	GClstr	0.202550	PHOT	0.000
0704	2MASX J03460305+0100064	0.186147	1	167	WHL J034603.0+010006	GClstr	0.181200	PHOT	0.008
0755	SDSS J113800.88+521303.9	0.296018	1	16	SDSSCGB 65403	GGroup	⋯	⋯	1.104
1002	2MASX J10535662+5909155	0.198533	1	26	WHL J105356.6+590915	GClstr	0.210650	PHOT	0.001
1023	2MASX J09254889+0745051	0.172306	2	22	GMBCG J141.45380+07.75151	GClstr	0.129650	PHOT	0.000
					MSPM 09586	GClstr	0.134320	SPEC	1.323
					SDSSCGA 00090	GGroup	0.134000	SPEC	1.872
1088	SDSS J140138.37+263527.6	0.284036	1	2	ZwCl 1359.5+2650	GClstr	⋯	⋯	1.902
1166	2MASX J22295446−0921345	0.279639	1	2	MaxBCG J337.47710−09.35962	GClstr	0.237650	PHOT	0.000
1268	2MASX J12005393+4800076	0.278617	2	47	GMBCG J180.22479+48.00211	GClstr	0.252000	PHOT	0.001
1270	SDSS J125157.99+305422.3	0.230703	3	14	MaxBCG J192.99166+30.90620	GClstr	0.283550	PHOT	0.001
1304	2MASX J16014061+2718161	0.164554	3	164	GMBCG J240.41924+27.30444	GClstr	0.193000	PHOT	0.000
					MaxBCG J240.43568+27.30263	GClstr	0.164750	PHOT	0.883
					WHL J160144.6+271809	GClstr	0.162200	PHOT	0.892
1329	2MASX J16273931+3002239	0.259761	1	19	GMBCG J246.91981+30.01418	GClstr	0.261000	PHOT	1.588
1420	2MASX J13475962+3227100	0.223113	1	16	SDSSCGB 16827	GGroup	⋯	⋯	0.748
1520	2MASX J12354859+3919078	0.237013	1	13	SDSSCGB 36014	GGroup	⋯	⋯	1.743
1549	2MASX J08464747+0446053	0.241509	1	20	WHL J084647.5+044605	GClstr	0.237650	PHOT	0.000
1559	CGCG 122−067	0.089008	5	310	MSPM 05544	GClstr	0.089190	SPEC	0.001

Notes.
[a] Number of galaxies within 1 Mpc and 500 km s^{-1}.
[b] Number of galaxies within 10 Mpc and 5000 km s^{-1}.
[c] Redshift type, from NED or reference therein. EST—estimated, PHOT—photometric, and SPEC—spectroscopic.
[d] Separation (in arcminutes) of the cluster or group catalog position in NED from the super spiral or super lenticular. In many cases the separation is zero because the brightest galaxy (i.e., the super spiral) position was apparently used to define the cluster position.

Table 9
Super Spiral and Lenticular Mergers and Interacting Pairs

OGC	Merger	Features	Companion	z_2	Sep. (″)	Sep. (kpc)[a]
0044	2 nuclei	⋯	SDSS J140722.29+135250.3	0.28601	2.0	9.0
0290	major pair	ν shape	SDSS J123429.74+515639.8	⋯	16.0	72.0
0299	major triple	⋯	SDSS J090944.05+222605.4	⋯	11.0	46.0
	⋯	⋯	SDSS J090944.08+222632.2	0.28380	27.0	115.0
0425	2 nuclei	debris	⋯	⋯	2.0	6.0
0516	major triple	⋯	SDSS J144753.90+144701.2	⋯	14.0	48.0
	⋯	⋯	SDSS J144752.76+144728.7	⋯	27.0	95.0
0574	2 nuclei	⋯	2MASX J12114871+6625146	⋯	3.0	12.0
0581	major pair	⋯	SDSS J134229.89+002138.1	⋯	19.0	74.0
0612	2 nuclei	⋯	SDSS J093540.00+565324.0	⋯	3.0	13.0
0749	2 nuclei	⋯	SDSS J155910.19+382626.9	⋯	4.0	15.0
0755	2 nuclei	ring	⋯	⋯	1.0	4.0
0789	2 nuclei	tail	⋯	⋯	5.0	14.0
0799	major pair	ring	SDSS J104723.75+230923.4	⋯	19.0	58.0
0909	2 nuclei	⋯	⋯	⋯	4.0	15.0
0968	2 nuclei	⋯	⋯	⋯	3.0	11.0
0983	2 nuclei	ring	SDSS J153618.68+452238.8	⋯	9.0	32.0
0984	major pair	⋯	SDSS J133740.61+494023.5	0.27221	28.0	115.0
1002	2 nuclei	⋯	⋯	⋯	3.0	9.0
1088	2 nuclei	tail	SDSS J140138.83+263530.6	⋯	7.0	30.0
1094	2 disks	⋯	SDSS J163357.74+172836.1	⋯	5.0	20.0
1182	2 nuclei	⋯	SDSS J004959.22−085332.0	⋯	10.0	21.0
1196	minor pair	ring	SDSS J154949.79+234452.2	⋯	17.0	69.0
1250	minor pair		SDSS J123212.17+102121.9	⋯	44.0	125.0
1304	2 nuclei	⋯	⋯	⋯	3.0	9.0
1329	nest	⋯	SDSS J162739.16+300217.7	⋯	7.0	28.0
	⋯	⋯	SDSS J162739.98+300227.5	⋯	9.0	38.0
1352	minor pair	⋯	SDSS J101605.14+303751.3	⋯	16.0	61.0
1375	2 nuclei	tail	SDSS J001550.69−100243.4	⋯	8.0	25.0
1395	2 nuclei	tail	SDSS J131039.16+223506.9	⋯	5.0	18.0
1409	2 nuclei	ring	SDSS J151720.48+603301.9	⋯	4.0	17.0
1420	2 nuclei	⋯	⋯	⋯	5.0	17.0
1423	minor pair	ν shape	SDSS J215251.02+122156.1	⋯	10.0	40.0
1457	major pair	tail	SDSS J093815.80+104500.9	⋯	16.0	60.0
1464	2 nuclei	⋯	SDSS J100416.17+295839.9	⋯	5.0	21.0
1500	2 nuclei	ring	⋯	⋯	4.0	14.0
1501	2 nuclei	debris	SDSS J093347.52+211434.0	⋯	4.0	12.0
1514	2 nuclei	⋯	SDSS J080316.86+325930.9	⋯	3.0	13.0
1549	2 nuclei	debris	SDSS J084647.56+044559.9	⋯	5.0	20.0
1554	major pair	ring	SDSS J134227.34+115707.0	⋯	31.0	131.0
1559	2 nuclei	debris	⋯	⋯	4.0	6.0
1562	2 nuclei	tail	⋯	⋯	1.0	4.0
1600	2 nuclei	tail	⋯	⋯	2.0	9.0
1608	minor pair	⋯	SDSS J040423.64−054135.7	⋯	11.0	43.0

Note.
[a] Projected separation.

ORCID iDs

Patrick M. Ogle https://orcid.org/0000-0002-3471-981X
Lauranne Lanz https://orcid.org/0000-0002-3249-8224
Philip N. Appleton https://orcid.org/0000-0002-7607-8766

References

Alatalo, K., Bitsakis, T., Lanz, L., et al. 2017, ApJ, 843, 9
Alatalo, K., Cales, S. L., Appleton, P. N., et al. 2014, ApJL, 794, L13
Bamford, S. P., Nichol, R. C., Baldry, I. K., et al. 2009, MNRAS, 393, 1324
Barkhouse, W. A., Green, P. J., Vikhlinin, A., et al. 2006, ApJ, 645, 955
Bell, E. F., & de Jong, R. S. 2000, MNRAS, 312, 497
Bell, E. F., McIntosh, D. H., Katz, N., & Weinberg, M. D. 2003, ApJS, 149, 289
Blanton, M. R., Hogg, D. W., Bahcall, N. A., et al. 2003, ApJ, 592, 819
Bogdan, A., Lovisari, L., Kovacs, O. E., et al. 2018, ApJ, 869, 105
Bressan, A., Panuzzo, P., Buson, L., et al. 2006, ApJL, 639, L55
Brinchmann, J., Charlot, S., White, S. D. M., et al. 2004, MNRAS, 351, 1151
Bruzual, G., & Charlot, S. 2003, MNRAS, 344, 1000
Burns, J. O., Hallman, E. J., Brennan, G., Motl, P. M., & Norman, M. L. 2008, ApJ, 675, 1125
Cava, A., Bettoni, D., Poggianti, B. M., et al. 2009, A&A, 495, 707
Chabrier, G. 2003, PASP, 115, 763
Chang, Y.-Y., van der Wel, A., da Cunha, E., & Rix, H.-W. 2015, ApJS, 219, 8
Conselice, C. J., Gallagher, J. S., III, & Wyse, R. F. G. 2001, ApJ, 559, 791
da Cunha, E., Charlot, S., & Elbaz, D. 2008, MNRAS, 339, 1595
Davari, R. H., Ho, L. C., Mobasher, B., & Canalizo, G. 2017, ApJ, 836, 75
de Jong, R. S. 1996, A&A, 313, 377
Dekel, K., & Birnboim, Y. 2006, MNRAS, 368, 2
Edge, A. C., Smith, G. P., Sand, D. J., et al. 2003, ApJL, 599, L69
Egami, E., Misselt, K. A., Rieke, G. H., et al. 2006, ApJ, 647, 922
Eisenstein, D. J., Annis, J., Gunn, J. E., et al. 2001, AJ, 122, 2267
Elbaz, D., Daddi, E., Le Borgne, D., et al. 2007, A&A, 468, 33
Faisst, A. L., Carollo, C. M., Capak, P. L., et al. 2017, ApJ, 839, 71

Falco, E. E., Kurtz, M. J., Geller, M. J., et al. 1999, PASP, 111, 438
Fraser-McKelvie, A., Brown, M. J. I., Pimbblet, K. A., et al. 2016, MNRAS, 4612, L11
Governato, F., Willman, B., Mayer, L., et al. 2007, MNRAS, 374, 1479
Guzzo, L., Schuecker, P., Bohringer, H., et al. 2009, A&A, 499, 357
Hernandez-Toledo, H. M., Vazquez-Mata, J. A., Martinez-Vazquez, L., Choi, Y. Y., & Park, C. 2010, AJ, 139, 2525
Hopkins, P. F., Bundy, K., Croton, D., et al. 2010, ApJ, 715, 202
Hopkins, P. F., Cox, T. J., Younger, J. D., & Hernquist, L. 2009, ApJ, 691, 1168
Hopkins, P. F., Hernquist, L., Cox, T. J., et al. 2006, ApJS, 163, 1
Lin, Y.-T., Shen, Y., Strauss, M. A., Richards, G. T., & Lunnan, R. 2010, ApJ, 723, 1119
Lintott, C. J., Schawinski, K., Bamford, S., et al. 2011, MNRAS, 410, 166
Lintott, C. J., Schawinski, K., Slosar, A., et al. 2008, MNRAS, 389, 1179
Lotz, J. M., Jonsson, P., Cox, T. J., & Primack, J. R. 2008, MNRAS, 391, 1137
Martig, M., Bournaud, F., Teyssier, R., & Dekel, A. 2009, ApJ, 707, 250
Masters, K. L., Mosleh, M., Romer, A. K., et al. 2010, MNRAS, 405, 783
Melnick, J., & De Propris, R. 2013, MNRAS, 431, 2034
Ogle, P. M., Lanz, L., Nader, C., & Helou, G. 2016, ApJ, 817, 109
Posti, L., Fraternali, F., & Marasco, A. 2019, A&A, 626, 56
Rines, K., Geller, M. J., Kurtz, M. J., et al. 2001, ApJ, 561, 41
Rodriguez-Gomez, V., Pillepich, A., Sales, L. V., et al. 2016, MNRAS, 458, 2371
Rowan-Robinson, M., Babbedge, T., Surace, J., et al. 2005, AJ, 129, 1183
Rykoff, E. S., Koester, B. P., Rozo, E., et al. 2012, ApJ, 746, 178
Schawinski, K., Urry, C. M., Simmons, B. D., et al. 2014, MNRAS, 440, 889
Schlafly, E. F., & Finkbeiner, D. P. 2011, ApJ, 737, 103
Sheth, K., Elmegreen, D. M., Elmegreen, B. G., et al. 2008, ApJ, 675, 1141
Simard, L., Mendel, J. T., Patton, D. R., Ellison, S. L., & McConnachie, A. W. 2011, ApJS, 196, 11
Skrutskie, M. F., Cutri, R. M., Stiening, R., et al. 2006, AJ, 131, 1163
Springel, V., & Hernquist, L. 2005, ApJL, 622, L9
Strauss, M. A., Weinberg, D. H., Lupton, R. H., et al. 2002, AJ, 124, 1810
Tremonti, C. A., Heckman, T. M., Kauffmann, G., et al. 2004, ApJ, 613, 898
Veron-Cetty, M.-P., Balayan, S. K., Mickaelian, A. M., et al. 2004, A&A, 414, 487
Wright, E. L., Eisenhardt, P. R. M., Mainzer, A. K., et al. 2010, AJ, 140, 1868
York, D. G., Adelman, J., Anderson, J. E. Jr., et al. 2000, AJ, 120, 1579